

Microstructural inhomogeneity and anisotropic properties in IN-718 structures fabricated by Electron Beam Melting

Mikrostrukturell inhomogenitet och anisotropa egenskaper i strukturer av IN-718 tillverkade genom Electron Beam Melting

Sebastian Brandtberg

Division of Engineering Materials

Department of Management and Engineering

Linköping University

June 5, 2017



Master thesis, 30 ECTS | Mechanical Engineering - Engineering Materials
Linköping university | Department of Management and Engineering
Spring 2017 | ISRN: LIU-IEI-TEK-A--17/02739—SE

Examiner

Mikael Segersäll

Supervisors

Johan Moverare (*Linköping University*)

Camilla Söderström (*Exova Materials Technology AB*)

Olov Johansson Berg (*Exova Materials Technology AB*)

Abstract

Additive Manufacturing, or 3D printing, provides an opportunity to manufacture advanced 3D geometries with little material waste and reduced need for tooling compared to conventional methods. There are, however, challenges remaining regarding anisotropy in the mechanical properties of built components.

The aim of this project is to investigate the anisotropy of additive manufactured material and the effect of different build directions. The material used is Inconel 718, which was manufactured by Electron Beam Melting as vertical and horizontal rods. The tests performed are microstructural investigations about the grains, precipitates and porosities, but also include hardness testing and tensile testing. The material is tested in its as-built state.

The results show that the material consist of an anisotropic microstructure with elongated grains in the build direction. The build height has a bigger influence on the properties of the material than the build direction for the specimens. The top pieces are consistently different from the others and are the least homogeneous. The microstructure consists of large quantities of delta-phase, and solidification pores are found throughout the material. The hardness of the material differs from 324 HV to 408 HV depending on the part of the build. The tensile testing shows that the vertically built specimens have a higher yield-strength and ultimate tensile strength while the horizontally built specimens have a greater ductility.

Preface

This report is written as a Master thesis in Mechanical Engineering at Linköping University (LiU). The project was carried out at the Division of Engineering Materials on the Department of Management and Engineering (IEI) as well as at Exova Materials Technology AB in Linköping (Exova). The project is set up by LiU and Exova.

I would like to thank my supervisors at Exova Camilla Söderström and Olov Johansson Berg and my supervisor at LiU Johan Moverare for good cooperation and support during the project. I would also like to thank Jonas Olsson at University West for constructing my material and sharing his knowledge about the EBM-process with me. I would also like to thank the entire MMS department at Exova for being helpful and friendly during my project.

Sebastian Brandtberg

Content

1	Introduction	1
1.1	Corporate presentation	1
1.2	Background	1
1.3	Formulation of questions.....	2
1.4	Scope.....	2
2	Theory.....	3
2.1	Additive manufacturing	3
2.1.1	Electron beam melting	4
2.2	Superalloys.....	7
2.2.1	Inconel 718.....	7
2.3	Microscopy.....	9
2.3.1	Light optical microscopy.....	9
2.3.2	Electron microscopy	10
2.4	Hardness testing	11
2.4.1	Vickers hardness test.....	11
2.5	Tensile testing	12
3	Method	14
3.1	Production of material	14
3.1.1	Metal powder	15
3.1.2	Build parameters	15
3.2	Specimen preparation.....	16
3.2.1	Cutting and molding	17
3.2.2	Grinding, polishing & etching	17
3.2.3	Test specimens	17
3.3	Microstructure investigation	18
3.3.1	Grains	18
3.3.2	Phases and precipitates.....	19
3.3.3	Porosities	19
3.4	Hardness testing	19
3.5	Tensile testing	19
4	Results	20
4.1	Microstructure	20
4.1.1	Grains	20
4.1.2	Phases and precipitates.....	21
4.1.3	Porosities	24
4.2	Hardness testing	28
4.3	Tensile testing	29
4.3.1	Tensile testing at RT	29
4.3.2	Tensile testing at 650 °C.....	31
5	Discussion	34
5.1	Microstructure	34

5.1.1	Grains	34
5.1.2	Phases and precipitates.....	34
5.1.3	Porosities	36
5.2	Hardness	37
5.3	Tensile testing	38
5.4	Source of errors	40
5.5	Future research.....	41
5.5.1	Future prospects	41
5.6	Resource utilization and environmental impact.....	42
6	Conclusions	43
7	References	44

Appendix 1 – Drawing of EBM Build (University West)

Appendix 2 – Drawing of test specimen for tensile testing (Linköping University)

Appendix 3 – Grain size evaluation, results

Appendix 4 – Hardness testing, results

Appendix 5 – Tensile testing results, complete

Figures

Figure 2.1. EBM-machine.....	3
Figure 2.2. Arcam A2X, EBM-machine.....	4
Figure 2.3. A schematic figure describing strongly elongated grains in a material.....	5
Figure 2.4. Directional solidification.....	6
Figure 2.5. Cross-sectional view of the melt pool.....	6
Figure 2.6. a) FCC crystal structure. b) BCT crystal structure.....	8
Figure 2.7. An orthorhombic structure.....	9
Figure 2.8. A comparison of the resolution for different microscopy methods.....	10
Figure 2.9. Vickers hardness test.....	12
Figure 2.10. An example of a stress-strain curve.....	13
Figure 3.1. Computer model of build.....	14
Figure 3.2. Built material in the process of abrasive blasting.....	14
Figure 3.3. The metal powder used in the EBM-machine.....	15
Figure 3.4. Build strategy.....	16
Figure 3.5. As received end pieces.....	16
Figure 3.6. As received tensile specimen.....	16
Figure 3.7. Cutting of end pices.....	17
Figure 3.8. Finished mold after grinding and polishing.....	17
Figure 3.9. Grain size evaluation.....	19
Figure 4.1. The shape of the grains.....	20
Figure 4.2. Difference in grain size in Mold 8.....	21
Figure 4.3. SEM of etched specimen from Mold 2.....	21
Figure 4.4. SEM using BSE-mode of etched and unetched specimen.....	22
Figure 4.5. Amount of precipitates in grain boundaries in $H_{close} \perp$ to the BD.....	22
Figure 4.6. Amount of precipitates in grain boundaries in $H_{away} \perp$ to the BD.....	23
Figure 4.7. Dendrites in top surface. LOM image from Mold 10 \parallel to the BD.....	23
Figure 4.8. Dendrites in V_{top}	24
Figure 4.9. Porosities in the interface between contour and hatch.....	24
Figure 4.10 Porosity in the interface between contour and hatch.....	25
Figure 4.11. SEM image of porosities in Mold 8.....	25
Figure 4.12. a) single porosity extending into the material. b) A LOM image of porosities.....	26
Figure 4.13 Cluster of porosities in V_{top}	26
Figure 4.14 Characteristic image of lines of pores in $V_{bottom} \perp$ to the BD.....	27
Figure 4.15 Lines of pores in H specimen \perp to the BD.....	27
Figure 4.16. Average Hardness value.....	28
Figure 4.17. Hardness results with lowest and highest result in each position removed.....	29
Figure 4.18. Tensile testing at room temperature stress-strain curve with all six specimens.....	30
Figure 4.19. Tensile testing at room temperature, stress-strain for the horizontally built specimens.....	30
Figure 4.20. Tensile testing at room temperature, stress-strain for the vertically built specimens.....	31
Figure 4.21. Tensile testing at 650 °C, stress-strain curve with all six specimens.....	32
Figure 4.22. Tensile testing at 650 °C, stress-strain for the horizontally built specimens.....	32
Figure 4.23. Tensile testing at 650 °C, stress-strain for the vertically built specimens.....	33
Figure 5.1. Direction of melt lines in horizontal rods.....	40

Tables

Table 2.1. Composition specifications of IN-718	8
Table 3.1. Composition of used IN-718 powder.	15
Table 3.2. List of tensile specimens used in the tensile testing.....	18
Table 3.3. List of molds.	18
Table 4.1. Average grain sizes.	20
Table 4.2. Visual examination of amount and distribution of porosities in the hatch	26
Table 4.3. Average hardness value for each position.	28
Table 4.4. Results from tensile testing at room temperature	29
Table 4.5. Results from tensile testing at 650 °C	31
Table 5.1. Compilation of hardness values for IN-718.....	38
Table 5.2. Summary of tensile behavior from studies conducted on as-built IN-718	39

Nomenclature

γ	Gamma
γ'	Gamma prime
γ''	Gamma double prime
δ	Delta
HV	Hardness (Vickers) [kgf/mm ²]
d	Diagonal length [mm]
P	Force [kgf]
$\dot{\epsilon}$	Strain rate [min ⁻¹]
F	Load [N]
σ	Stress [MPa]
ϵ	Strain [%]
E	Young's modulus [MPa]
$\sigma_{y0,2\%}$	Offset yield strength of 0,2% [MPa]
σ_{UT}	Ultimate tensile strength [MPa]
A_0	Initial cross section area [m ²]
l_i	Gauge length [m]
l_0	Initial gauge length [m]
ϵ_f	Elongation at failure [%]
	Parallel
⊥	Perpendicular

Abbreviations

AM	Additive Manufacturing
BCT	Body-Centered Tetragonal
BD	Build Direction
BSE	Backscattered Electrons
CAD	Computer-Aided Design
DF	Dark Field
DIC	Differential Interference Contrast
DS	Directional Solidification
EBM	Electron Beam Melting
EDS	Energy Dispersive Spectroscopy
FCC	Face-Centered Cubic
H	Horizontal
HIP	Hot Isostatic Pressing
IN-718	Inconel 718
LMD	Laser Metal Deposition
LOM	Light Optical Microscopy
RT	Room Temperature
SE	Secondary Electrons
SEM	Scanning Electron Microscopy
SiC	Silicon Carbide
SLM	Selective Laser Melting
TCP	Topologically Close-Packed
TEM	Transmission Electron Microscopy
TiN	Titanium Nitride
V	Vertical

1 Introduction

This project was carried out as a master's thesis at the Division of Engineering Materials at Linköping University in cooperation with Exova Materials Technology AB during the spring of 2017. This project was a part of a bigger project called Suman-Next, a 3-year project about additive manufacturing at University West in collaboration with multiple industrial partners, including Exova Materials Technology AB.

The objective of this project was to evaluate the microstructural inhomogeneity and anisotropic properties in the superalloy Inconel 718 (IN-718) fabricated by Electron Beam Melting (EBM). Tensile testing, microscopy studies and hardness testing were carried out. The long-term aim is to obtain a greater understanding of the EBM-process and its usability to manufacture high temperature materials.

1.1 Corporate presentation

Exova Materials Technology AB, hereinafter referred to as Exova, is a company that offers independent accredited testing, investigations and education in the areas of materials and processes. The company has an extensive technical competence within metallic materials, polymer materials, fuel and lubricants as well as non-destructive testing. Exova is active in several sectors, such as aerospace, defense, petrochemicals as well as energy and transportation ^[1].

For Exova, this master thesis is intended to create a basic understanding of additive manufacturing (AM) and more specifically the EBM process. Exova has expertise in material testing and failure analysis and AM has been identified as a process for the future. Exova therefore want to build a similar understanding of the material- and fracture properties of AM-manufactured details.

1.2 Background

Additive Manufacturing (AM), often called 3D printing, have with the use of the latest tools in computer-aided design (CAD) and the ability to conduct layer-by-layer fabrication gone from being a rapid prototyping tool to a rapid manufacturing tool with significantly improved quality ^[2]. What used to be a prototyping tool for polymers can now be used as a manufacturing method for high performance metals. There are many benefits with AM methods, for example are both the material waste and the need for tooling reduced and there is a possibility to manufacture highly advanced 3D geometries. Some geometries enabled by AM-technology are impossible to manufacture with traditional casting or forming methods. There are, however, some challenges remaining, in particular regarding anisotropy in the mechanical properties of built components. This leads to uncertainties about the predictability of the manufactured material ^{[3][4]}. A potential use of AM is Ni-based superalloys that could benefit from the advantages of the AM-technology. However, there are currently only limited data available for Ni-based superalloys manufactured through AM ^[5].

This study is based on the material IN-718; today's most used superalloy on the market ^[6]. It aims to broaden the knowledge about IN-718 fabricated by EBM. An increased understanding of its anisotropic behavior would lead to a safe and a predictable use of the material for numerous applications. In the future, it might be possible to use the anisotropies

as something positive and manufacture components with tailored material properties to optimize the individual performance for each specific part.

1.3 Formulation of questions

The questions to be answered in this report are:

- How does the build direction (BD) affect the microstructure and the mechanical properties of the material?
- Are the microstructural characteristics dependent on the build height?
- How does the hardness of the material correlate to the microstructure?
- How does elevated temperature affect the tensile properties of the material?

1.4 Scope

This project is a master thesis comprising of 30 ECTS credits, corresponding to 800 hours. This makes time the main limitation of this project. The availability of testing equipment is also limited during the period of time, in which this project is carried out. The project is limited to evaluate the build material by the BD as a variable parameter and only in its as-built condition. The other process parameters are kept constant. The tensile testing at elevated temperatures will not exceed 650 °C due to significantly increased equipment wear at higher temperatures.

2 Theory

2.1 Additive manufacturing

Additive manufacturing, or AM, refers to technology that creates a 3D object by layer-by-layer fabrication, commonly called 3D-printing. Contrary to conventional production methods where material is subtracted from a workpiece, AM-methods add material and are able to create a complex component with little need for pre-production tooling and a minimal amount of waste material^{[7][4]}. The foundation of the process is a CAD-model divided into thin layers then built by an AM machine.

AM for metals have in the last years moved from being a rapid prototyping tool to a rapid manufacturing tool, the feedstock commonly used is powder or wire. There are many new AM-techniques developed, but the ones most promising for the industry today is Selective Laser Melting (SLM), Electron Beam Melting (EBM) and Laser Metal Deposition (LMD). SLM and EBM are both metal powder based fusion techniques^[8] where a metal-powder is spread out on a bed and then melted according to the design by a laser or an electron beam, respectively. The newly built layer is lowered and a new powder layer is added for the next layer. After the manufacturing, the unused powder is removed and can after processing be used again. This method cannot be used for closed cellular structures, which would trap metal powder inside the structure. LMD differs from the other two by adding material, in the form of powder or wire, and melting it at the same time see Figure 2.1a allowing larger build volumes and a higher build rate^[2].

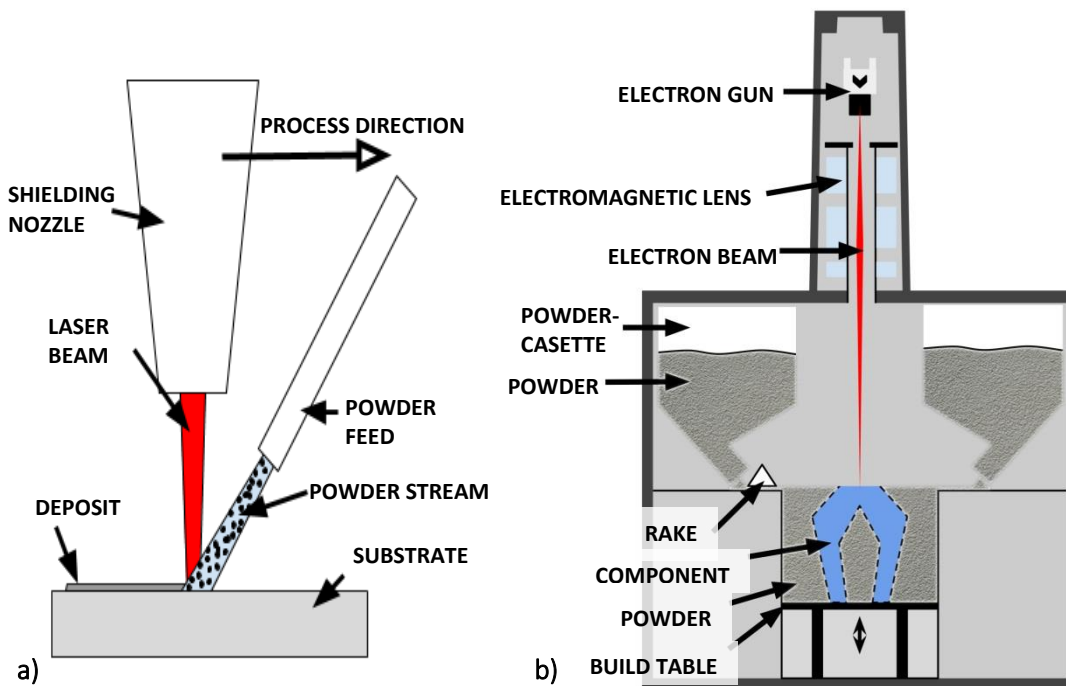


Figure 2.1. a) LMD process. A representation of the process where a powder is added and melted simultaneously onto a substrate. b) EBM-machine. A schematic visualization of an EBM-machine and its main parts

2.1.1 Electron beam melting

EBM is an AM technology that creates 3D components using a high-powered electron beam. It is mainly focused on space- and high temperature applications and medical implants ^[9]. EBM is a registered trademark by Arcam AB based in Mölndal, Sweden.

The EBM-machine, Figure 2.1b, consists of an electron gun, which generates an electron beam. The beam is focused and guided by electromagnetic lenses allowing the beam to be scattered across the powder bed or focused to melt a specific part of the powder. The lower part of the machine is the build chamber which is kept in a vacuum of 1×10^{-5} mbar. A partial pressure of He to 2×10^{-3} mbar can also be introduced that enhances heat conduction and cooling of the component. There are two powder cassettes where the metal powder is stored before it is used in the process and a rake used to distribute it. At the bottom of the chamber is a build table that is lowered during the process, on which the component is manufactured. Figure 2.2 shows an Arcam A2X system where the computer control is in the left module and the EBM is in the right ^{[10][11]}.

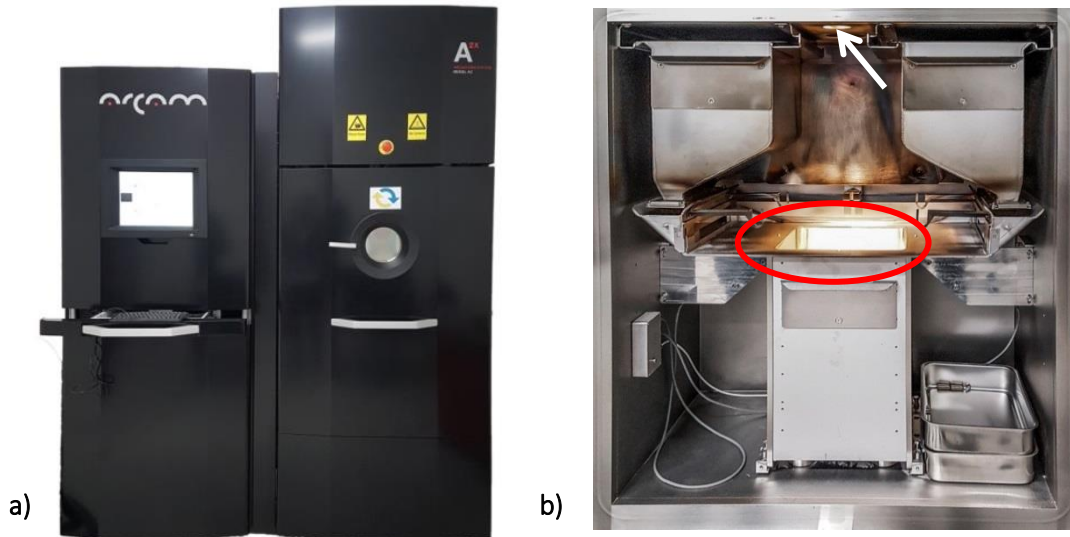


Figure 2.2. a) Arcam A2X, EBM-machine. Computer control on the left and the EBM in the right module. b) Build chamber of an EBM-machine without the presence of powder. The arrow marks where the electron beam enters the build chamber and the circle marks the build table start position. The build table is submerged in the picture.

Photographs by Olov Johansson Berg, used with permission

2.1.1.1 Process description

The first step of the EBM process is heating of the build chamber and build table. After the initial heating, a thin layer of metal powder is added to the build table. The powder is then sintered by a diffuse beam ^[12]. This helps to prevent the powder from scattering ^[13]. When the wanted sintering temperature is reached the melting of the powder starts. A highly focused electron beam selectively melts the powder according to the CAD-model creating a 2D cross section of the geometry of the component. The electron beam scans over the material and generate melt pool temperatures reaching several thousand degrees for a short fraction of time before returning to the elevated process temperature ^[14]. Since the process temperature is high throughout the build, the residual stresses in the component is minimized, which in turn results in less distortion and less need of support structures and anchors in the build. This could be compared to the stress relief that cast superalloys are usually put through after

manufacturing ^[15]. The build table is lowered one powder layer thickness and new powder is raked, creating the next layer, which is to be sintered and then selectively melted. This iterative process continues until the complete component is manufactured on the build table, which now is submerged, as shown in Figure 2.2b ^[16]. When the component is finished, it is cooled down while remaining in the machine. To cool the component down the previously mentioned He-gas is induced to increase the thermal transport ^[12]. Abrasive blasting is used to get rid of the residual powder when the component is removed from the machine.

2.1.1.2 Microstructure

The resulting microstructure in a component fabricated with EBM often consists of strongly elongated grains parallel to the BD, shown in Figure 2.3. As shown in several studies ^{[4][16][17][18]}, this anisotropic microstructure reoccurs in a number of materials. In the EBM process, many heating cycles of the material promotes grain growth where growth often is favored along one crystallographic orientation. For example in an austenitic material, the $\langle 100 \rangle$ direction is the most favorable. The grains with one of their $\langle 100 \rangle$ directions aligned with the thermal gradient along the BD will be favoured over the other grains and will be overrepresented in the finished component ^[19].

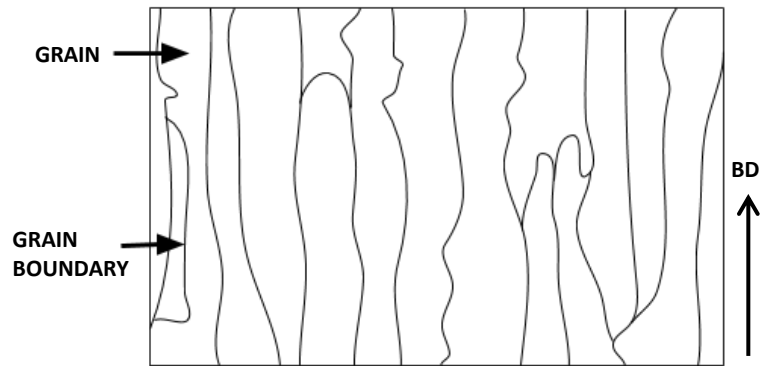


Figure 2.3. A schematic figure describing strongly elongated grains in a material

This kind of microstructure is present in material produced by another production method, casting using Directional Solidification (DS). DS was developed as a way to control the microstructure in a cast material ^[20]. Today DS is used to enhance a components fracture resistance and resistance to creep and is used for instance in turbine blades. The same method is used when manufacturing single crystal components when only one grain is allowed to grow the full length of the component leaving a finished piece completely free of grain boundaries ^[21]. One method of DS is shown in Figure 2.4 where a melt is slowly removed from a furnace creating cooling on one side and heating on the other, resulting in a temperature gradient along which the grains grow ^[22]. The EBM-process can be compared to this because of the constant reheating of the top layers that creates a thermal gradient inside the build chamber from the build surface and downwards to the submerged build plate.

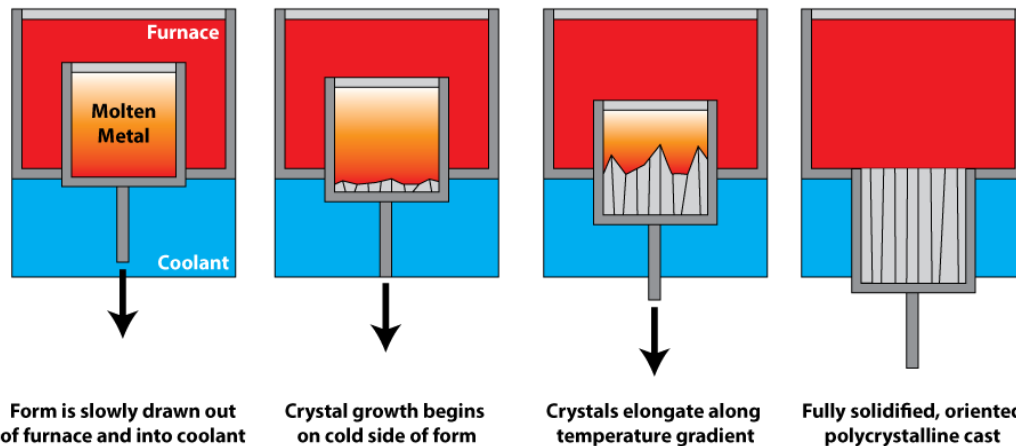


Figure 2.4. Directional solidification. A schematic of the process where molten metal is slowly taken out of a furnace creating a temperature gradient making grains propagate upwards. Created by Jedelbrock, used under CC BY-SA 4.0, <https://commons.wikimedia.org/w/index.php?curid=47268760>

2.1.1.3 Build parameters

When using EBM, different parameters affect the microstructure of the manufactured component; build temperature, scan strategy and number of other process parameters are important. With a large variety of parameters, each step of the process can be altered by multiple factors. For example when a component experience problems with porosity or cavities, a larger melt pool volume could be a solution. This can be done by the use of a slower deflection speed, increasing the beam power or by a combination of both ^[23]. The shape of the melt pool can be altered which will affect the underlying layers and the overlap of the electron beam. A highly focused beam will penetrate deeper into the material and add more heat to underlying layers, while a defocused beam will result in a wider, but shallower, melt pool as shown in Figure 2.5. The defocused beam will produce a lower temperature in the melt pool and will vaporize less material ^[17].

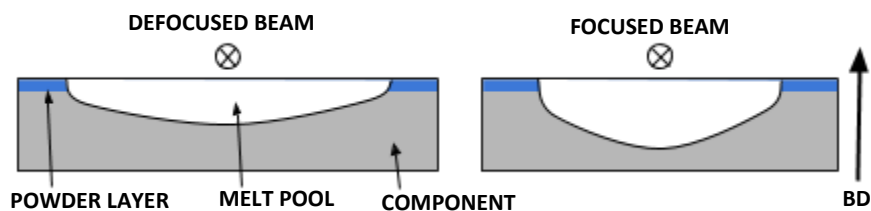


Figure 2.5. Cross-sectional view of the melt pool perpendicular to the direction of the electron beam motion, marked with the crossed circle in the picture. The defocused beam provides a shallower and wider melt pool than the focused beam

Powder quality can also be of great importance in the EBM process. Defects in the powder can include satellites on the surface of the powder particles and variations in shape and size of the particles. All affect the properties of the powder. There can also be gas-filled porosities in the powder, which may cause inclusions of gas in the final part. The cooling of a component can also have a big impact in the quality, especially for materials with sensitive phase-transformations in the used temperature range. The size and shape of a component can also play an important role since they both affect the cool rate. An alternative, slower, cool down process than the one mentioned in 2.1.1.1 has been studied where the component is left in the vacuum of the machine taking 10-20 hours to cool down. This may result in a variation in the microstructure of the manufactured component ^[12].

2.1.1.4 A comparison to Selective Laser Melting

Both EBM and SLM belong to the metal powder based fusion techniques. The two methods completely melt the material unlike other powder based fusion techniques, which use sintering to fuse the powder. What differentiates the methods in addition to what kinetic energy source used, is that SLM uses an inert gas in the building chamber and only melts the powder used for the build. When the component is complete, the residual powder can easily be removed. The EBM process works in vacuum and heats the whole powder bed but only melts the powder used for the build. This leads to some sintering taking place in the residual powder that needs to be removed using abrasive blasting. The positive aspect of using an elevated temperature is that it results in less residual stresses. Hot Isostatic Pressing (HIP) can be used on the manufactured component to get rid of any porosities. A better result is obtained by EBM due to the underpressure remaining in cavities in the material. The pores in a SLM manufactured part contain trapped gas making them harder to cave in^[14]. EBM is also capable of a higher build rate than the SLM, while SLM provides a better surface finish and quicker cooling^{[16] [23] [24]}.

2.2 Superalloys

A superalloy is a material group intended for high-temperature applications. The first superalloys were designed to be used in jet engines, which requires a material of high strength at high temperatures^[25]. Today superalloys have a number of different uses such as heat exchangers, rockets and turbines. To be able to operate at elevated temperatures a material needs to maintain good properties at temperatures close to its melting point. They should have an ability to operate at above 0.6 of the melting temperature, which means that a material with a melting point of 1200 °C can be operated at over 700 °C. There are three types of superalloys: Ni-, Fe- or Co-based. In addition to the base material, they all have a large amount of alloying elements intended to obtain even better material properties. The materials used for the highest temperature are the Ni-based superalloys, which have the highest strength and best creep- and corrosion resistance^{[6] [26] [27]}.

2.2.1 Inconel 718

IN-718 is a Ni-based superalloy used up to about 650 °C. It has good weldability for a high-strength material and excellent strength properties^{[28] [29]}. IN-718 is one of the most widely used superalloys today, and has been for several decades. It combines a low cost with good properties and availability, and it has become the standard material for the majority of gas turbine discs^[6]. IN-718 is also used in cryogenic conditions due to good properties at low temperatures^[30], and in aerospace industry for jet engines. For example in the CF6 engine by GE Aircraft Engine, IN-718 comprise over one third of the finished component weight^[31].

2.2.1.1 Composition

The composition specifications of IN-718 are presented in Table 2.1. One of the differences to other Ni-based superalloys is the high amount of Fe in the material, often more than 17 wt. %^{[32] [33] [34]}. Even though IN-718 is classified as a Ni-based superalloy, it is sometimes listed as a Ni-Fe-based superalloy due to the high Fe content^[6].

Table 2.1. Composition specifications for IN-718^[35]

Element	wt. %
Ni	50,00-55,00
Cr	17,00-21,00
Fe	Balance
Nb+Ta	4,75-5,50
Mo	2,80-3,30
Ti	0,65-1,15
Al	0,20-0,80
Co	1,00 max.
C	0,08 max.
Mn	0,35 max.
Si	0,35 max.
P	0,015 max.
S	0,015 max.
B	0,006 max.
Cu	0,30 max.

2.2.1.2 Microstructure

The microstructure of IN-718 consists of a number of different phases. This is an account for the most common phases and their features.

Gamma & gamma prime

The continuous matrix is called gamma (γ) and consists primarily of Ni and is the same for all Ni-based superalloys. γ is an austenitic phase with a face-centered cubic (FCC) crystal structure^[6], Figure 2.6a. Another phase with an FCC-structure is the gamma prime (γ') phase, which is coherent to the γ -phase. The γ' -phase consists mainly of Ni and Al (Ni_3Al), but may contain some Ti as well, shown in Figure 2.6a. It is often the principal strengthening phase of Ni-based superalloys, however for IN-718, γ' only accounts for a small part of the strengthening^{[28] [26]}.

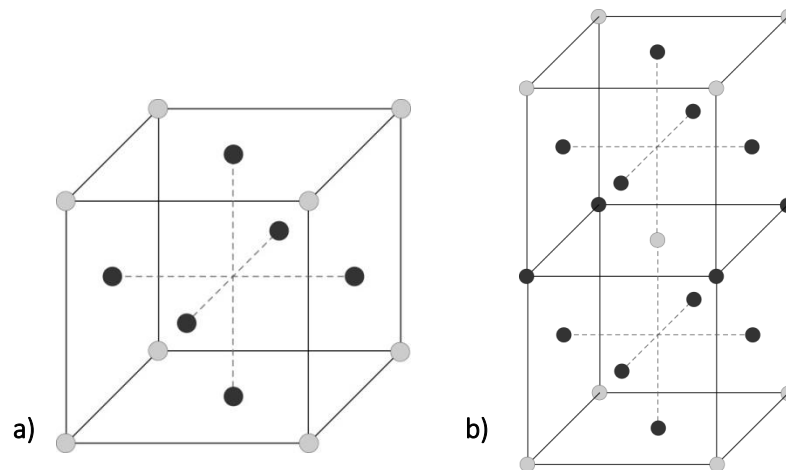


Figure 2.6. a) FCC crystal structure. In γ -phase, Ni constitutes all atoms in the structure. In γ' -phase, Ni constitutes the dark atoms in the figure and Al/Ti the lighter corner atoms. b) BCT crystal structure. In γ'' -phase, Ni constitutes the dark atoms in the figure and Nb the lighter atoms

Gamma double prime & delta

A main contributor to the strength of the material at temperatures up to 650 °C, is a phase called gamma double prime (γ''). γ'' form precipitates in and is coherent with the γ -matrix^[36]. The γ'' is the main strengthening phase of IN-718 and consists of Ni and Nb (Ni_3Nb) in a body-centered tetragonal (BCT) crystal structure Figure 2.6b^[37]. γ'' form as disc-shaped particles with a diameter of around 50 nm and is starting to become unstable at temperatures exceeding 650 °C. The γ'' -hardened IN-718 also has the delta (δ) phase present (Ni_3Nb), which is of an orthorhombic structure, shown in Figure 2.7. In small amounts, the δ -phase helps to control the grain sizes and optimizing the fatigue and tensile properties. Formation of too much δ -phase leads to degradation of the properties of the material because of its incoherency with the γ -phase^[38]. Since γ'' can transform into δ at higher temperatures, a careful heat treatment is necessary to ensure the formation of γ'' -phase and not δ -phase^[39]^[26]^[6].

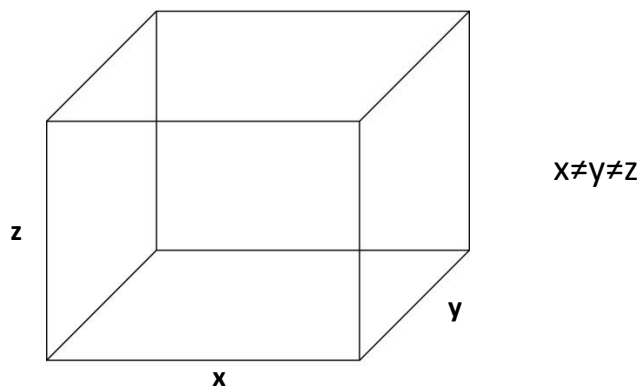


Figure 2.7. An orthorhombic structure, meaning the three dimensions of the cube (x,y,z) are all of different lengths

Other phases

Other phases that can be found in IN-718 are different types of carbides. Carbides can be found in many different forms, for example precipitated as cells on grain boundaries, as films or as lamellae. The carbides forming on the grain boundaries may prevent grain boundary sliding and therefore strengthen the material, they can also enhance the high temperature creep performance of a material. There are also undesirable phases formed called topologically close-packed (TCP) phases, which are usually brittle and often appear as plate- or needle-shaped. The most discussed ones for IN-718 are sigma and laves phases that both lead to decreased mechanical properties when occurring in more than trace amounts^[26]^[6].

2.3 Microscopy

2.3.1 Light optical microscopy

Light Optical Microscopy (LOM) is a method where a sample is exposed to light and studied either through an ocular or through a computer software. In biological fields the use of transmission optical microscopy is the most common, where light shines through thin slices of biological tissue of which to be examined. In the field of metallurgy, the light is instead reflected on the surface of the material. Contrasts are created through topological differences on the surface or through optical effects in the material that affect the reflected light.

2.3.1.1 Sample preparation

A good preparation of the sample is essential to be able to study the material. This could prove problematic because one method can get a different response depending on what material the sample consists of. The preparation often includes casting a test piece in a mold. The specimen can then be ground flat and polished. The most common grinding media is Silicon Carbide (SiC), diamond or alumina all of which are available in various sizes. A coarser size is used to begin with and then slowly working towards smaller sizes. Water is applied during the grinding to cool the material and remove debris from the abrasive paper. After the grinding, polishing of the test piece is commenced. This could be done either mechanically, chemically or electrochemically. The polishing remove damages to the test piece afflicted from previous steps and provides a mirror-like finish to the piece. The final step is etching which selectively remove material chemically. For example, one way is to use an agent that reacts with the grain boundaries in the material depressing them, which then makes the grains more visible in the LOM^[40].

2.3.2 Electron microscopy

Ernst Ruska and Max Knoll invented the first electron microscope in 1931. Since then the electron microscope has been developed into a sophisticated instrument capable of distinguishing individual atoms. Today there are several different types of electron microscopes, including Scanning Electron Microscopy (SEM) that uses an electron beam to scan the surface of a sample. Another is Transmission Electron Microscopy (TEM) that uses a high voltage electron beam to irradiate a thin sample. SEM and TEM have a superior resolution over LOM, shown in Figure 2.8. The theoretical limit of the resolution is the emissions wavelength, for LOM it is the one of visible light, which is 390 to 700 nm. An electron, at an acceleration voltage of 100 kV, has a wavelength of 0,004 nm. For comparison, a hydrogen atom radius is about 0,04 nm. The resolution limit for SEM and TEM are today not the wavelength of the emission, instead the main limitation is the lens system used^[41].

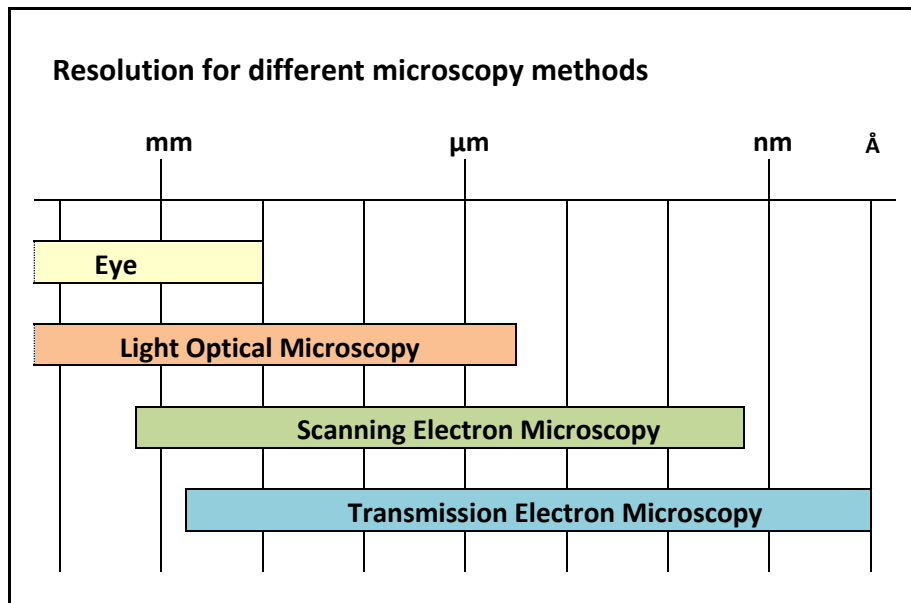


Figure 2.8. A comparison of the resolution for different microscopy methods

2.3.2.1 Scanning electron microscopy

SEM, like EBM, operates in vacuum using an electron beam focused by a number of electromagnetic lenses. The beam is directed onto the surface of the sample and has a better depth of field compared both to the TEM and the LOM. Since the electron beam will not penetrate the sample, a number of detectors are placed to catch electrons and photons emitted from the surface of the sample.

In a SEM, the information is obtained from electrons and photons generated by the electron beam scanned on the specimen. Information can be obtained from a number of sources. The primary information given is from Secondary Electrons (SE) and Backscattered Electrons (BSE). The SE are low-energy electrons originating from the top layers of the substrate knocked out of their orbit by the incident electrons. These will mainly give topographic information of the sample. The BSE are high-energy electrons originating from the electron beam being reflected back from the specimen. They contain information of the composition of the specimen and can provide crystallographic information^[42]. Other signals that can be generated and detected in SEM include x-rays, Auger electrons, cathodoluminescence and absorbed specimen current. These other signals can also provide some information on both the topographic and composition of the specimen. They could also provide information on the electronic, optic and radiative properties as well as information about defects in the material^[40].

2.4 Hardness testing

Hardness is a measurement of a material's resistance to indentation of its surface. There are a number of test methods for hardness, the most common are Rockwell, Vickers and Brinell, all of which have their own hardness scale^[21]. The methods are similar among the three where a small ball or a sharp tip is pressed into the material with a specific force. The hardness is then decided from the indent left in the material. This means that the methods provide a measurement of a material's tendency to resist plastic deformation, the elasticity properties of the material are not tested.

There are other contexts where hardness testing refers to other things, such as resistance to scratching of the surface, where Mohs scale of mineral hardness is used^[43]. The method is a subjective scale only comparing minerals to each other. Today Mohs scale is often used to demonstrate the resistance to scratches on hardened glass used for example in mobile devices.

2.4.1 Vickers hardness test

Vickers hardness test was developed in 1921 as an alternative to the Brinell method. It is one of the widest hardness scales and can be used on all metals. Vickers hardness test uses a diamond indenter shaped like a square-based pyramid with a tip angle of 136° to press into the sample, see Figure 2.9. The hardness of the material is denoted HV and calculated using the size of the indent (d_1 & d_2) and the force used (P) using Equation (1) & (2)^[44].

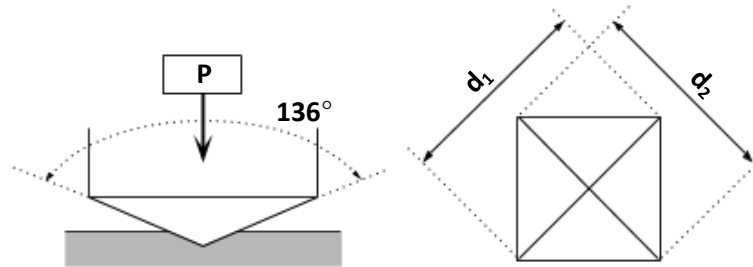


Figure 2.9. Vickers hardness test. On the left, the indenter is pressed in to the material. On the right, the shape of the indentation left in the material

$$HV = Constant \times \frac{\text{Test force}}{\text{Area of indentation}} = 0,102 \times \frac{2P \sin \frac{136^\circ}{2}}{d^2} = 0,1891 \times \frac{P}{d^2} \quad (1)$$

Where d is the mean diagonal length:

$$d = \frac{d_1 + d_2}{2} \quad (2)$$

2.5 Tensile testing

Tensile testing measures a materials resistance to an applied force. It can be used on a wide range of materials, both metals, alloys and plastics are commonly tested. For more brittle materials, like ceramics, other test methods are often preferred. The strain rate ($\dot{\epsilon}$) of a tensile test is often low. A test specimen is mounted in the tensile testing machine and an axial load (F) is applied. An extensometer or a strain gauge is used to measure the extension of the material.

The results of a tensile test is converted to size independent parameters, load is converted to stress (σ), Equation (3), and the extension of the material to strain (ϵ), Equation (4). A stress-strain diagram shown in Figure 2.10 is often used to visualize the results. The strain and stress are linearly proportional to each other in the beginning of the test, this is the elastic zone. The material will return to its initial shape if the sample is unloaded in the elastic zone. This proportional behavior is described by Hooke's law, Equation (5), and is referred to as the modulus of elasticity, or Young's modulus (E).

When a material reaches the end of the elastic zone, it will experience either plastic deformation or a fracture. Plastic deformation is non-reversible change of shape of a material, the transition between the elastic and plastic zone is called yield strength. Yield strength is defined as how resistant a material is to plastic deformation. An offset yield strength of 0,2% ($\sigma_{y0,2\%}$) is often used since the yield strength is hard to define in the stress-strain curve. The ultimate tensile strength (σ_{UT}) is the stress obtained at the highest applied load, after this point local deformation in the material will begin, called necking, and eventually lead to failure^[45].

$$\sigma = \frac{F}{A_0} \quad (3)$$

$$\varepsilon_i = \frac{l_i - l_0}{l_0} \quad (4)$$

$$E = \frac{\Delta\sigma}{\Delta\varepsilon} \quad (5)$$

Where A_0 is the initial cross section area, l_0 is the initial gauge length and l_i is the gauge length.

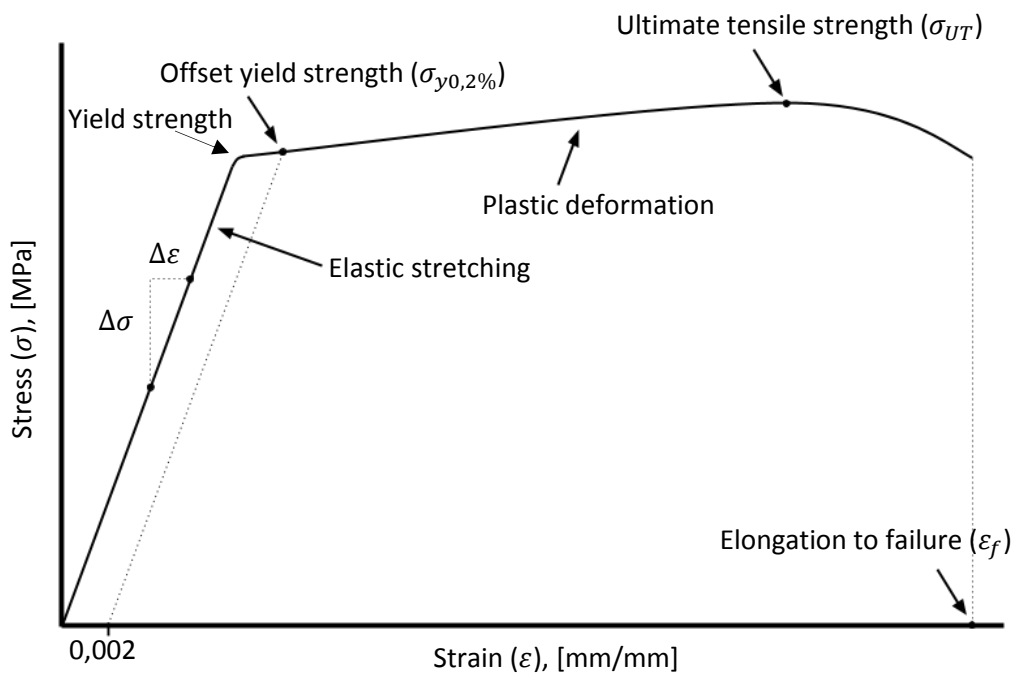


Figure 2.10. An example of a stress-strain curve. A elastic behavior in the beginning gives a linear appearance. The plastic deformation begins when the yield strength is reached

3 Method

3.1 Production of material

The material for this project was manufactured in an Arcam A2X EBM-machine at University West. The build, shown in Figure 3.1, consisted of circular rods oriented vertical (V) and horizontal (H). The vertical rods extend in the BD and the horizontal rods perpendicular to the BD. The rods were built with denotations at the ends, where XZ1-XZ9 are the horizontal rods and XY1-XY9 the vertical rods. The build also consisted of cubes, not related to this project. The cubes were built with enough space not to interfere with the building of the rods. A more detailed drawing can be found in Appendix 1.

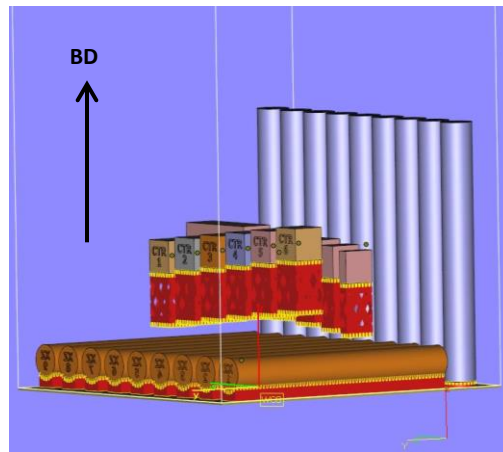


Figure 3.1. Computer model of build. The horizontal and vertical rods are a part of the project. Model by Jonas Olsson (University West), used with permission

Abrasive blasting was used to remove the excess powder after the build was complete, shown in Figure 3.2. The material has not been subjected to any post heat treatment. All parts of this project have used the material in its as-built condition.

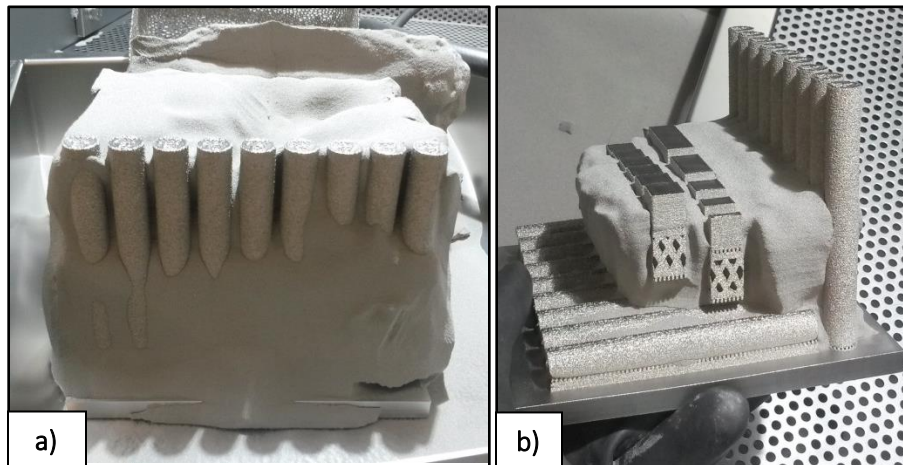


Figure 3.2. Built material in the process of abrasive blasting. a) Early in the post-process with most of sintered powder still remaining. b) Later in the process with all rods visible. Pictures by Jonas Olsson (University West), used with permission

3.1.1 Metal powder

The metal powder used in the EBM-process was supplied by Arcam AB under the name Arcam Inco 718 powder and have the chemical composition according to Table 3.1. All values are within the composition specification of IN-718 stated in Table 2.1.

Table 3.1. Composition of used IN-718 powder. All values within the specifications

Element	wt. %
Ni	54,11
Cr	19,0
Nb+Ta	4,97
Mo	2,99
Co	0,04
Ti	1,02
Al	0,52
Mn	0,12
Si	0,06
Cu	0,0
C	0,03
P	0,004
S	<0,001
B	<0,001
Ta	<0,01
Fe	Balance

A previous study of the used powder has shown that some satellites are present on the surface of the particles, shown in Figure 3.3 ^[46]. The powder size ranges from approximately 40 μm to 120 μm . The study of the powder was performed on unused powder. The build for this project was number eight in line of reused powder without any blending of new powder. This is due to an ongoing study by University West on the reusability of powder in the EBM process. The quality of the powder used in this study can therefore not be ensured.

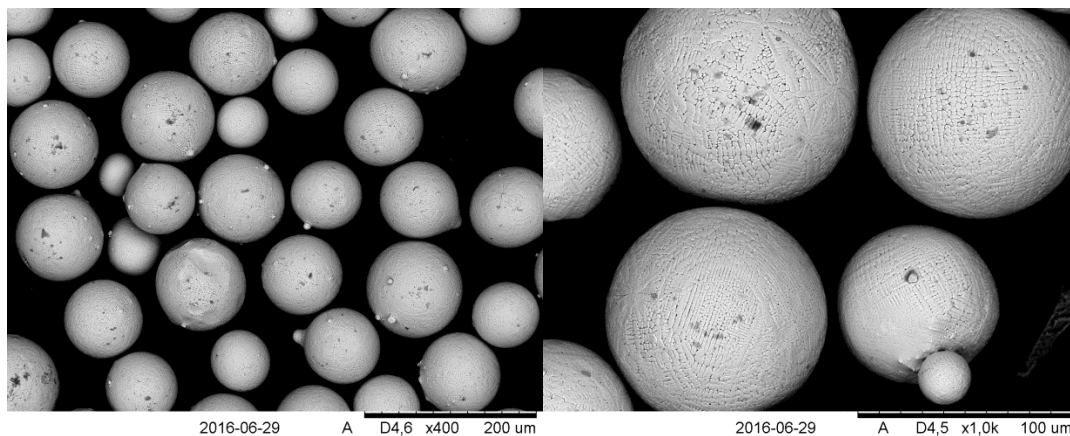


Figure 3.3. The metal powder used in the EBM-machine. Some satellites are visible on the surface of the powder particles. Pictures by Paria Karimi Neghlani (University West), used with permission

3.1.2 Build parameters

The scan strategy used in the build was a triple contour point melt where the layers are built from the outside in. The contour build is followed by a line melt of the hatch (the material inside the contour), shown in Figure 3.4. A line offset of 0,125 mm with a rotation of 180° was used for the hatch. The rotation means that the beam sweeps the material from opposite

directions on every other layer. The layer thickness was $75\ \mu\text{m}$ and a speed function index of 63 was used. The max current used was 18 mA and the focus offset was 15 mA. All Arcam's automatic functions for the EBM-machine were activated during the build, which means that current and speed is automatically adjusted for each layer and might not be constant.

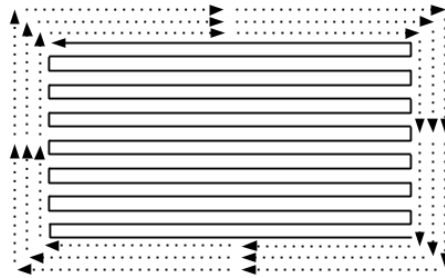


Figure 3.4. Build strategy. The dotted lines illustrate the three-layer contour. The filled line illustrates the line-melt for the hatch. Line offset for the hatch is $0,125\ \mu\text{m}$

3.2 Specimen preparation

Both end pieces on each of the manufactured rods were cut off. These pieces of about 1,5 cm on each side of the rod, shown in Figure 3.5, were intended for microscopy studies and hardness testing. The rest of the rod was intended for tensile testing and was sent away for machining according to the drawing in Appendix 2. An as-received tensile specimen is shown in Figure 3.6, the damage shown is typical for all the specimens received. The end pieces were prepared by cutting, molding and polishing. The hardness testing and microscopy was performed on 12 end pieces from six rods. The middle three horizontal (XZ4-XZ6) and the middle three vertical (XY4-XY6) of the nine rods were chosen.



Figure 3.5. As received end pieces. a) shows end pieces of vertical rod XY5, the last melt pool can be seen on the left part which is the top. b) shows vertical rod XZ5. c) shows XZ9 and a shrinking effect from the build leaving the end piece deformed



Figure 3.6. As received tensile specimen. Some damages from the machining of the specimen can be seen on the left elevation, marked in the figure

3.2.1 Cutting and molding

The first step was to cut the end pieces to expose the faces of the sample to be examined. As shown in Figure 3.7, two cuts were made. One circular surface and one square surface perpendicular to the circular was cast in a resin called PolyFast by Struers.

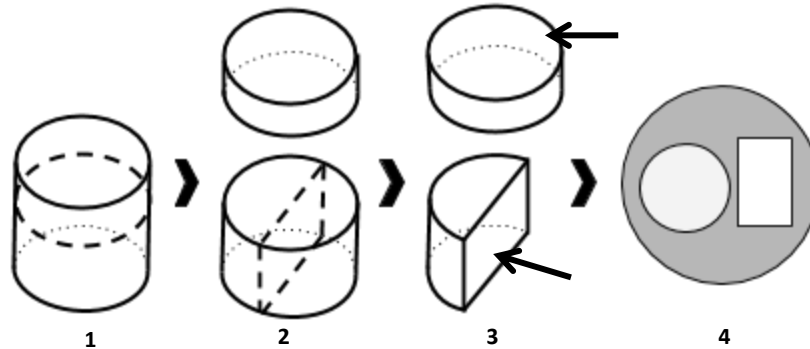


Figure 3.7. Cutting of end pieces. Step 1, the thick dotted line show the first cut. Step two, the thick dotted line show the second cut in the lower piece. Step 3 illustrates the two surfaces to be studied in the microscopy and hardness testing. The arrows point to the surfaces to be examined. Step 4, shows the surfaces from step 3, in a mold

3.2.2 Grinding, polishing & etching

The initial grinding was performed with a SiC paper #120 to get an even surface on the specimens. Following this step was a method recommended for Ni-based superalloys by Struers, method number 1429^[47]. This method includes four steps, two grinding steps with SiC paper #220 and MD-Largo with diamond suspension (9 μm). The two polishing steps used was 3 μm diamonds and a 0.04 μm colloidal silica polish. Most of the tests and investigations were performed on the polished surface, but for some investigations an etchant was used. The etching used was electrolytic in oxalic acid. A finished mold is shown in Figure 3.8.



Figure 3.8. Finished mold after grinding and polishing

3.2.3 Test specimens

The rods sent to be machined resulted in 18 tensile test specimens, nine horizontal and nine vertical. Two horizontal specimens were damaged in the machining process and two additional in the testing. The used specimens, listed in Table 3.2, were chosen because of their more uniform appearance. The selection of which samples to be tested at room temperature (RT) and at elevated temperature was random.

Table 3.2. List of tensile specimens used in the tensile testing

H (RT)	V (RT)	H (650 °C)	V (650 °C)
XZ5	XY1	XZ2	XY5
XZ1	XY9	XZ7	XY6
XZ6	XY7	XZ9	XY3

The surfaces described in 3.2.1 was molded and resulted in 12 molds with 2 surfaces in each as shown in Figure 3.7. One surface that shows the microstructure parallel (\parallel) to the BD and one perpendicular (\perp) to the BD. The molds are listed in Table 3.3. The position column is referring to which rod and where in the EBM-machine the samples were built. The vertical rods have one end in the bottom of the machine and one end at the top. The horizontal rods have one end close to the vertical rods, called “close” and one end on the other side of the build chamber, called “away”.

Table 3.3. List of molds. Which rods and which part of the rod they originate from

Mold №	Position	Specimen
1	H _{close}	XZ4
2	H _{away}	XZ4
3	H _{close}	XZ5
4	H _{away}	XZ5
5	H _{close}	XZ6
6	H _{away}	XZ6
7	V _{bottom}	XY4
8	V _{top}	XY4
9	V _{bottom}	XY5
10	V _{top}	XY5
11	V _{bottom}	XY6
12	V _{top}	XY6

3.3 Microstructure investigation

The microstructure was investigated by studying the grains, phases, precipitates and porosities in the material. The microstructure was examined using SEM and LOM. Both SE and BSE were used in the SEM. Energy Dispersive Spectroscopy (EDS) was used to get an idea of the composition of phases and precipitates. In LOM, Dark Field Illumination (DF) and Diffraction Interference Contrast (DIC) were used for some examinations to change the contrast in the image.

3.3.1 Grains

Polished samples examined in SEM were used for the study of grains. The SEM was set to backscatter mode with an acceleration voltage of 15 kV. Ten photos were taken on each specimen with a random distribution in the bulk of the material. Three lines of 400 μm were added to each photo at predetermined sites, shown in Figure 3.9. The number of grain boundaries that intersected the line was counted, which gave a mean value on the grain size. When examining the grain size, only the surfaces \perp to the BD were included. This direction shows the grains in the equiaxed direction and allows multiple measurements per picture.

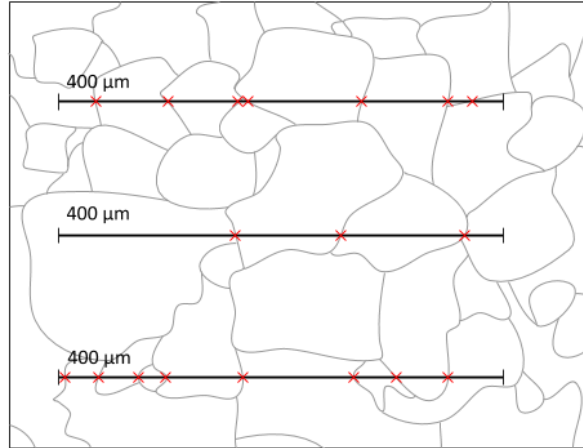


Figure 3.9. A schematic representation of how the lines were placed and grain boundaries that intersect the line was counted

3.3.2 Phases and precipitates

The phases and precipitates in the material have been studied both in etched and unetched specimens. EDS-analysis was used to obtain more information on the composition of the phases and precipitates.

3.3.3 Porosities

The amount of porosities has not been measured, but an overview of where and what kind of porosities that exist in the material have been made. The two types of porosities studied were gas-induced porosities and process induced porosities. Two types of process induced porosities were studied, lack of fusion and shrinkage porosities.

3.4 Hardness testing

A Qness Q10 A+ testing machine was used to perform the hardness testing. The method used was Vickers, HV1 meaning a force of 1 kgf was used (equivalent of 9,807 N). Five indents were made within the bulk material of each surface in the molds. The indents were placed further apart than three times the indentation diameter from one another and any edges according to the ISO 6507 standard ^[44].

3.5 Tensile testing

The tensile testing was performed on an Instron 5982 machine with a mounted oven. The used strain rate was 0,005 [mm / mm] min⁻¹ for all tests. Six specimens were tested at RT with an extensometer attached to the specimen using rubber bands. The extensometer was removed after a few percent elongation to ensure that it was not still attached when the specimen failed. After the extensometer was removed, the tests were run until fracture.

Tensile testing at elevated temperature was performed at 650 °C on six specimens. No extensometer was used. The specimens were heated to 650 °C, which took an average of 40 minutes. The specimens were allowed to soak for 20 minutes at the target temperature before the test began. A temperature increase of the oven was necessary during some of the tests to keep the specimen at the target temperature.

4 Results

4.1 Microstructure

Presented here are the findings made in the microstructural investigation.

4.1.1 Grains

The examination of the grains show strongly elongated grains in the BD. Figure 4.1 shows the two surfaces from Mold 12, both \parallel and \perp to the BD. The same feature is shown in all studied samples.

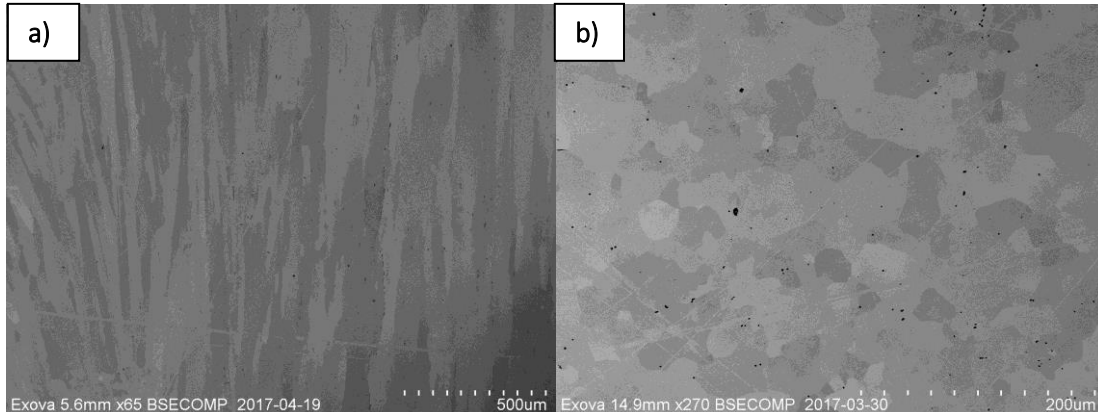


Figure 4.1. The shape of the grains. SEM picture of Mold 12. a) shows the surface \parallel to the BD with strongly elongated grains. b) shows the \perp surface to the BD with a more equiaxed appearance

4.1.1.1 Grain size determination

The average grain sizes for various positions in the build are presented in Table 4.1. The average values are based on 30 images with three measurement lines in each. Full results are found in Appendix 3. The scatter refers to the highest and lowest average on one picture, not the smallest and largest grain.

Table 4.1. Average grain sizes. The scatter derives from the highest and lowest average value from one picture not from individual grains or lines

Position	Average [μm]	Scatter [μm]
H, close	32	25 – 41
H, away	34	27 – 46
V, bottom	35	27 – 43
V, top	69	27 – 300

The scatter is large in V_{top} . If the two extremes are excluded a scatter of 41-200 μm is obtained. Figure 4.2 shows two different areas from Mold 8 with different grain sizes. Similar distributions are found in all V_{top} specimens.

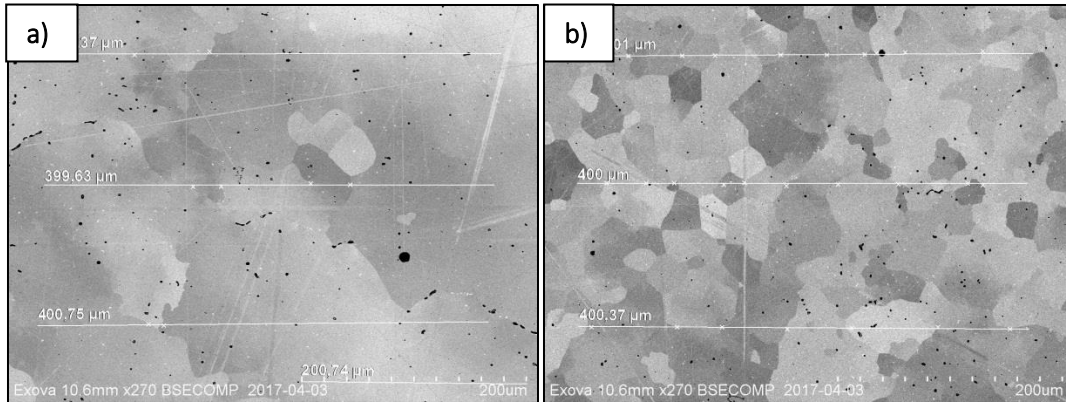


Figure 4.2. Difference in grain size in Mold 8 \perp to the BD. a) consists of large grains that are difficult to define while b) consist of smaller, more easily defined grains. Both images are taken on the same surface

4.1.2 Phases and precipitates

Presented here are pictures of phases and precipitates found in the material. Figure 4.3 shows an etched surface from Mold 2 taken in SEM. Figure 4.4a shows the same types of phases and precipitates in BSE-mode, making heavier elements appear lighter in color in the picture. Figure 4.4b is from Mold 4 and is unetched. The grain boundaries are visible and the larger precipitates are mostly concentrated along the grain boundaries. EDS-analysis establishes the larger precipitates in both Figure 4.3 and Figure 4.4 as Nb-rich. Similar results are obtained for the smaller precipitates as well but with a difficulty to get a good reading in the SEM, making these results uncertain.

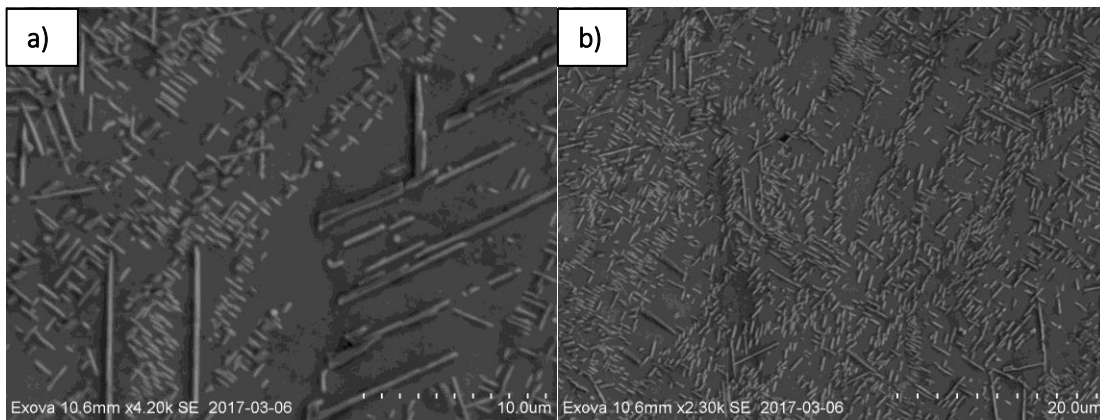


Figure 4.3. SEM of etched specimen from Mold 2 \parallel to the BD. Many precipitates in different sizes is present

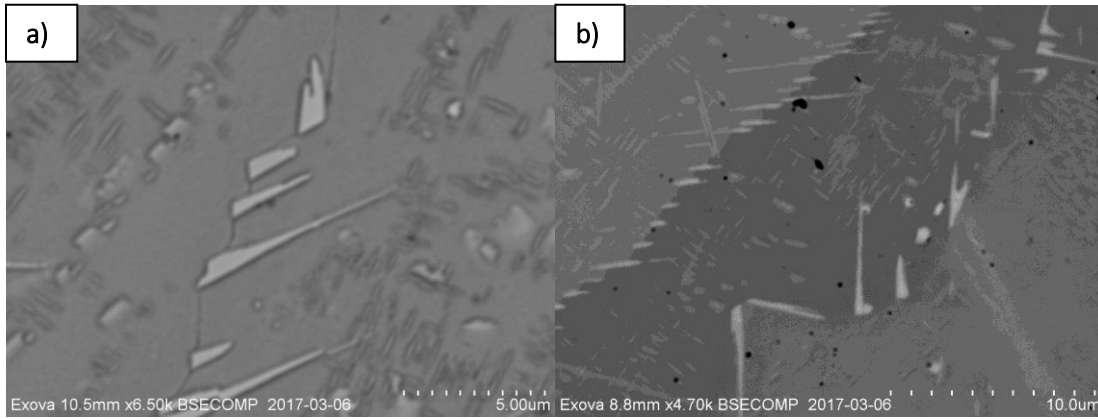


Figure 4.4. SEM using BSE-mode on etched and unetched specimen. a) is from Mold 2 \perp to the BD and is etched. b) is from Mold 4 and is unetched \parallel to the BD

Figure 4.5 shows an area from Mold 3 originating from H_{close} . Figure 4.6 shows Mold 4 and originates from H_{away} . A comparison between the two shows a big difference in size and number of precipitates along the grain boundaries. These pictures are representative of all studied specimens in each area. Samples originating from V_{bottom} are similar to those of H_{close} shown in Figure 4.5. In V_{top} , only few precipitates of this kind exist.

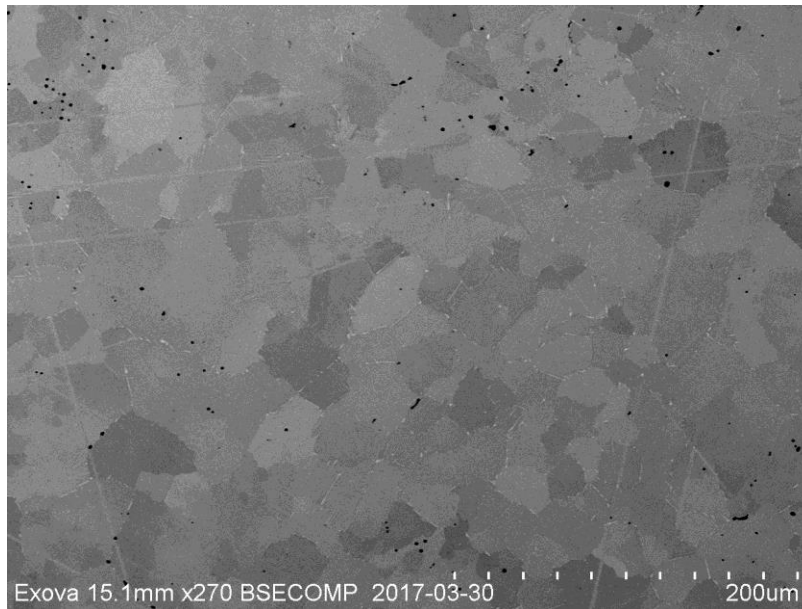


Figure 4.5. Amount of precipitates in grain boundaries in H_{close} \perp to the BD. SEM image from Mold 3

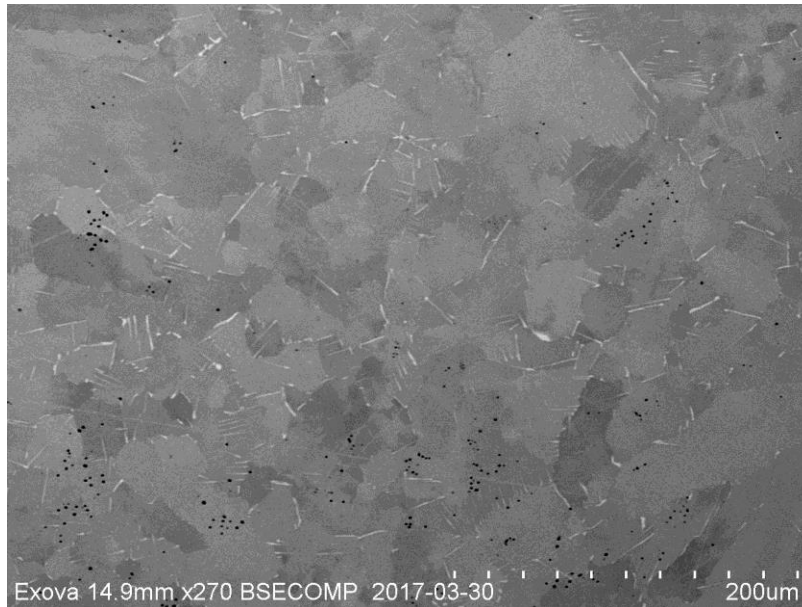


Figure 4.6. Amount of precipitates in grain boundaries in $H_{away} \perp$ to the BD. SEM image from Mold 4

4.1.2.1 Dendrites

Dendritic structures are found in the V_{top} specimens after etching. Figure 4.7 is from Mold 10 and captured with LOM. The horizontal lines are derived from the build of the part. The dendrites are directed along the BD. The shape of the dendrites can be seen in Figure 4.8, which uses DIC to highlight the texture of the surface. Precipitates are gathered in the interdendritic regions. EDS-analysis revealed many of them to contain high levels of Nb, and some precipitates contain high levels of Ti.

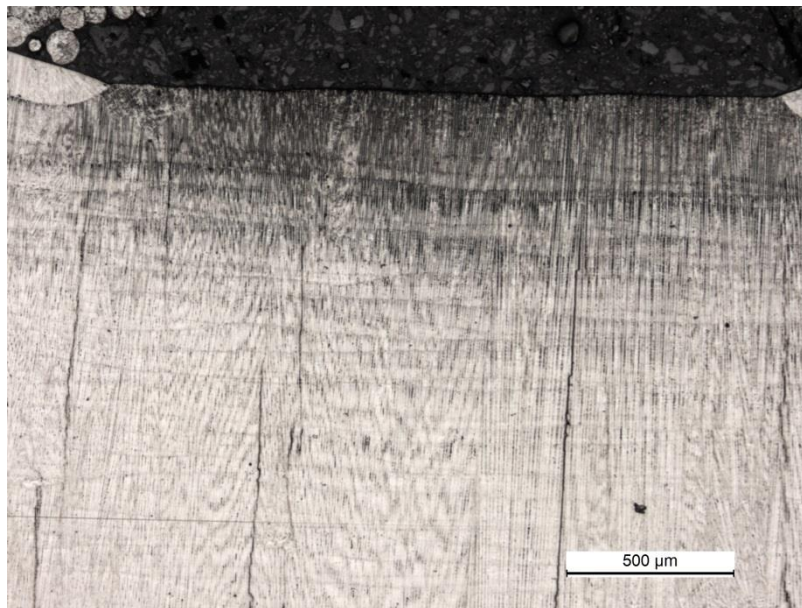


Figure 4.7. Dendrites in top surface. LOM image from Mold 10 \parallel to the BD

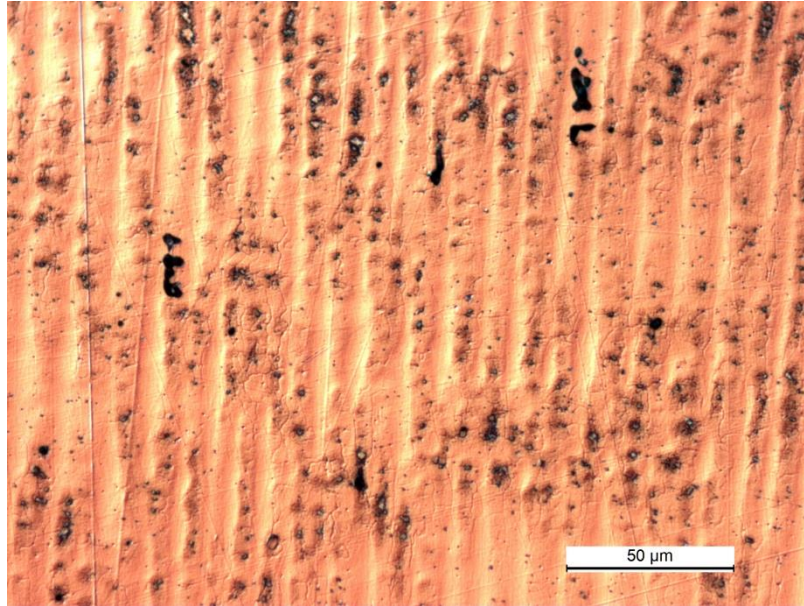


Figure 4.8. Dendrites in V_{top} . LOM image from Mold 10 // to the BD using DIC to highlight the texture in the surface. Most of the precipitates are found in the interdendritic regions

4.1.3 Porosities

Large porosities exist in the interface between the contour build and the hatch, as shown in Figure 4.9 and Figure 4.10. This kind of porosity is often of an irregular shape with distinguishable powder particles from the build. It has been found in many of the studied specimens, though most of them smaller in size compared to the ones presented in Figure 4.9 and Figure 4.10. Porosities marked with arrows in both pictures are completely round. These types of porosities are found in a few places in the material, but in random locations. All similar porosities are smaller than the size of individual powder particles.

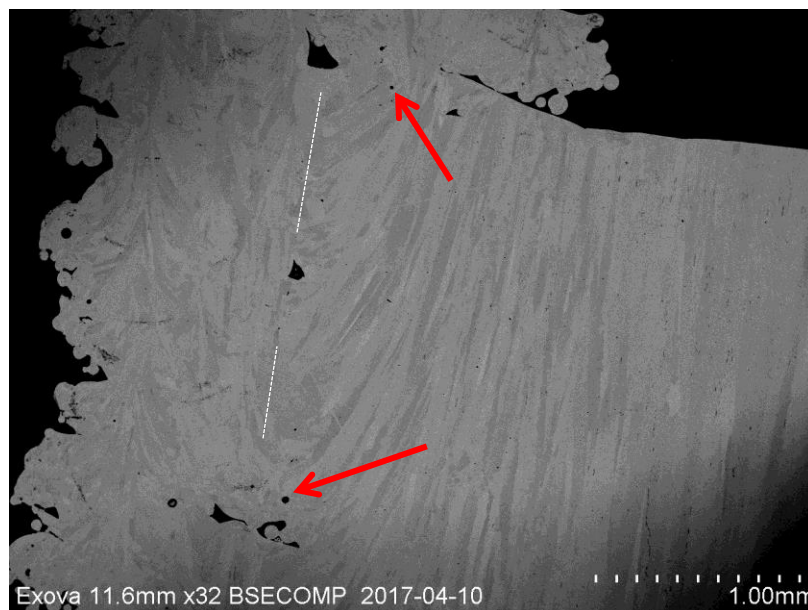


Figure 4.9. Porosities in the interface between contour and hatch. SEM image from Mold 8, // to the BD. A number of porosities are visible along the interface. Dotted white lines show approximate location of the interface. Arrows points out a circular porosities

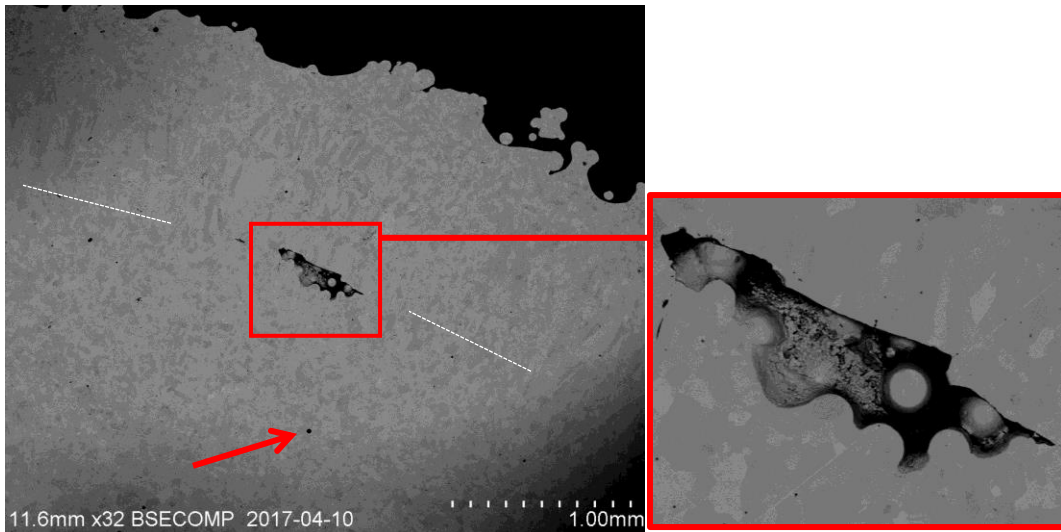


Figure 4.10 Porosity in the interface between contour and hatch. SEM image from Mold 8, \perp to the BD. The larger porosity, magnified to the right, displays partially melted powder particles. Dotted white lines show approximate location of the interface. Arrow points out a circular porosity

Most porosities observed are smaller and uneven in shape. Figure 4.11 shows an area with a high density of this kind of porosities from Mold 8. In the magnification to the right, the uneven shape of the porosities is clearly visible. An individual porosity which extends into the material is shown in Figure 4.12a. This image is taken \perp to the BD. Figure 4.12b is a LOM image from Mold 7 taken \parallel to the BD showing the pores extending in the BD.

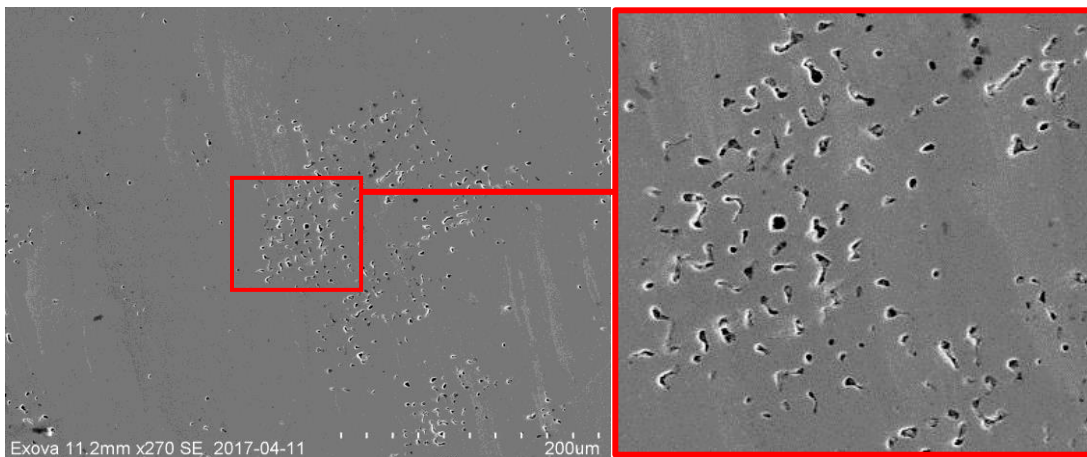


Figure 4.11. SEM image of porosities in Mold 8. Cluster of porosities \perp to the BD. The pores is of an uneven shape which is clearly visible in the magnification on the right

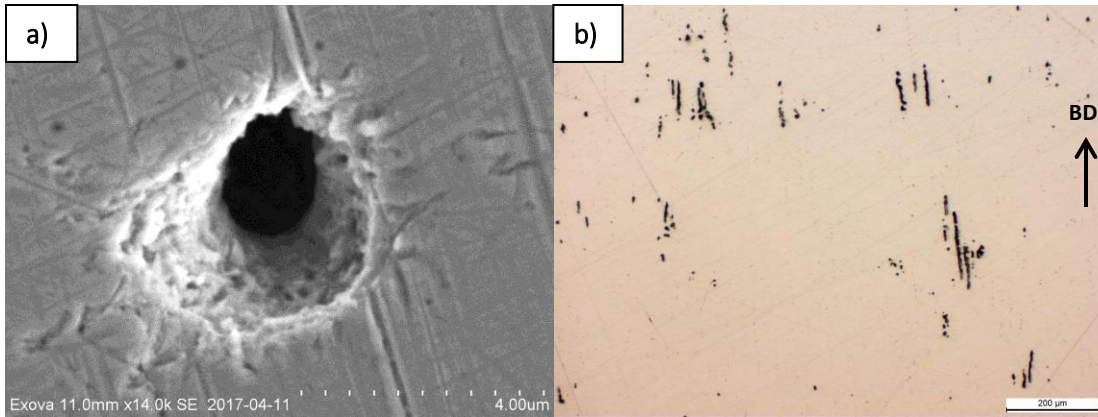


Figure 4.12. a) SEM image of a single porosity extending into the material. Image from Mold 3 taken \perp to the BD. b) A LOM image of porosities from Mold 7, \parallel to the BD. Porosities extend in the BD

The amount and distribution of the smaller kind of porosities was examined on surfaces \perp to the BD, the result is presented in Table 4.2. Figure 4.13 shows an area in V_{top} from Mold 8 with a high concentration of porosities. This kind of cluster is found in all V_{top} specimens, but not as dense as in the one shown.

Table 4.2. Visual examination of amount and distribution of porosities in the hatch, examined \perp to the BD

Position	Amount & Distribution
V_{top}	Porosities are highly concentrated to one or a few places in the hatch. In addition to these areas, the porosities are few and scattered.
V_{bottom}	Porosities forming clear lines evenly distributed over the hatch, as shown in Figure 4.14.
H_{away}	Fewer porosities than V_{bottom} but with the same linear pattern
H_{close}	Fewer porosities than V_{bottom} but with the same linear pattern

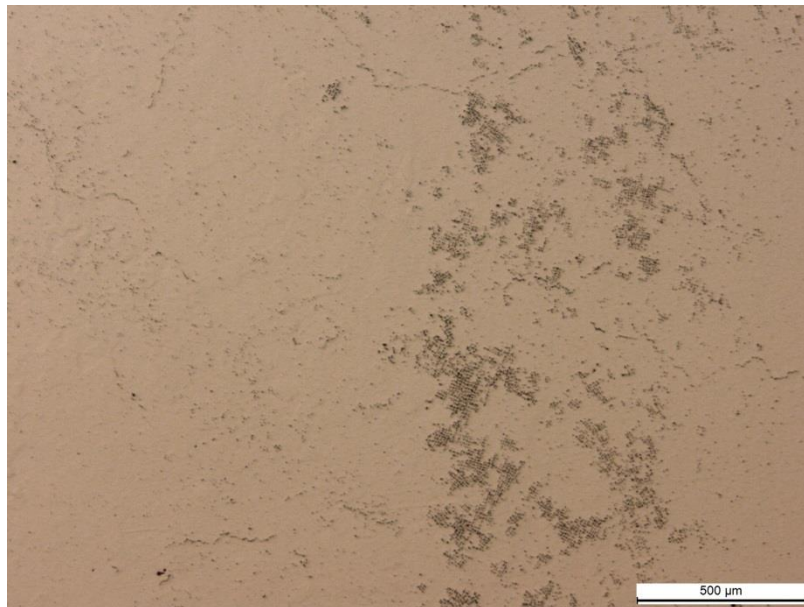


Figure 4.13 Cluster of porosities in V_{top} . LOM image from Mold 8, \perp to the BD. Image are showing the same cluster as Figure 4.11

Figure 4.14 displays the lines mentioned in Table 4.2, the image is from V_{bottom} in Mold 7. Similar lines are seen in most of the hatch and are representative for all V_{bottom} specimens. Figure 4.15 is from Mold 3, placed in H_{close} . The pattern of lines does not appear as clear as in Figure 4.14, DF imaging is used to visualize them. The porosities are fewer and less clustered, which is representative for all H-specimens studied. The distance between the lines is mostly between 200-300 μm but occurs in the range of 150-400 μm

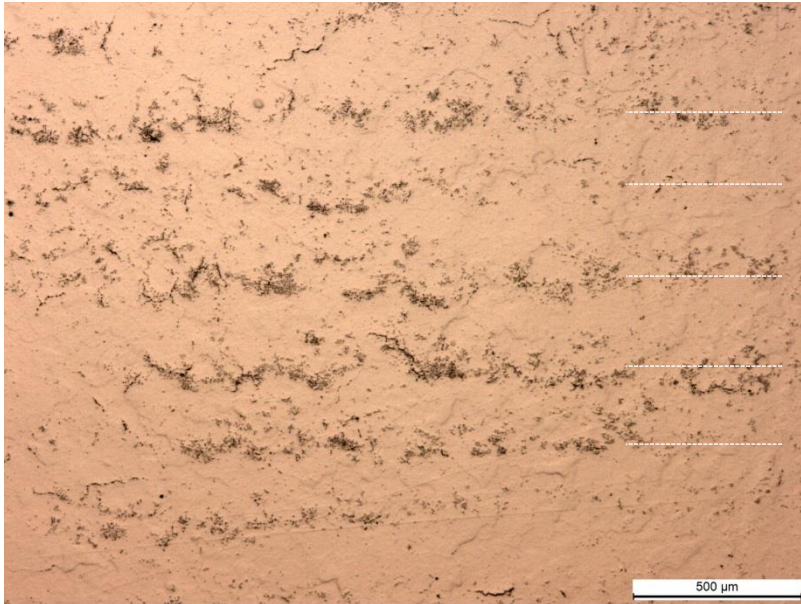


Figure 4.14 Characteristic image of lines of pores in V_{bottom} \perp to the BD . Dotted white lines show approximate location of lines of pores. Image from LOM image from Mold 7

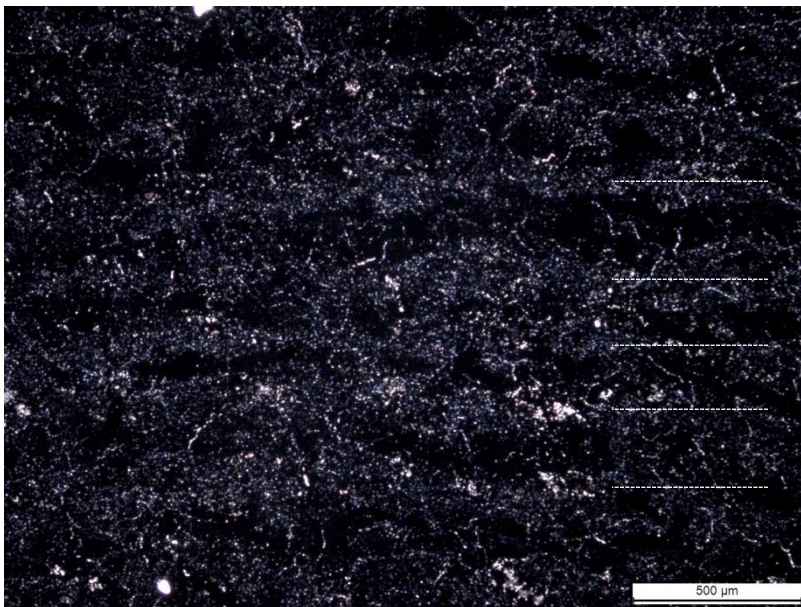


Figure 4.15 Lines of pores in H specimen \perp to the BD , fewer pores and more indistinct lines compared to V_{bottom} . DF imaging results in a better visualization of lines. Dotted white lines show approximate location of lines of pores. Image from Mold 3

4.2 Hardness testing

The results from the hardness testing are presented in Table 4.3 and Figure 4.16. The values are average values of all molds with the same position, the complete results can be found in Appendix 4. It can also be seen that the distribution of the results from the specimens in the same position was relatively even, most samples cover a large part of the total range. The alternative would be that the results from some samples are only in the upper part of the spectrum and some in the lower part.

Table 4.3. Average hardness value for each position. Measured on surfaces both \parallel and \perp to BD

Position	Surface to BD	Avg. Hardness [HV]
H _{away}	\parallel	324
	\perp	336
H _{close}	\parallel	356
	\perp	350
V _{bottom}	\parallel	372
	\perp	381
V _{top}	\parallel	414
	\perp	408

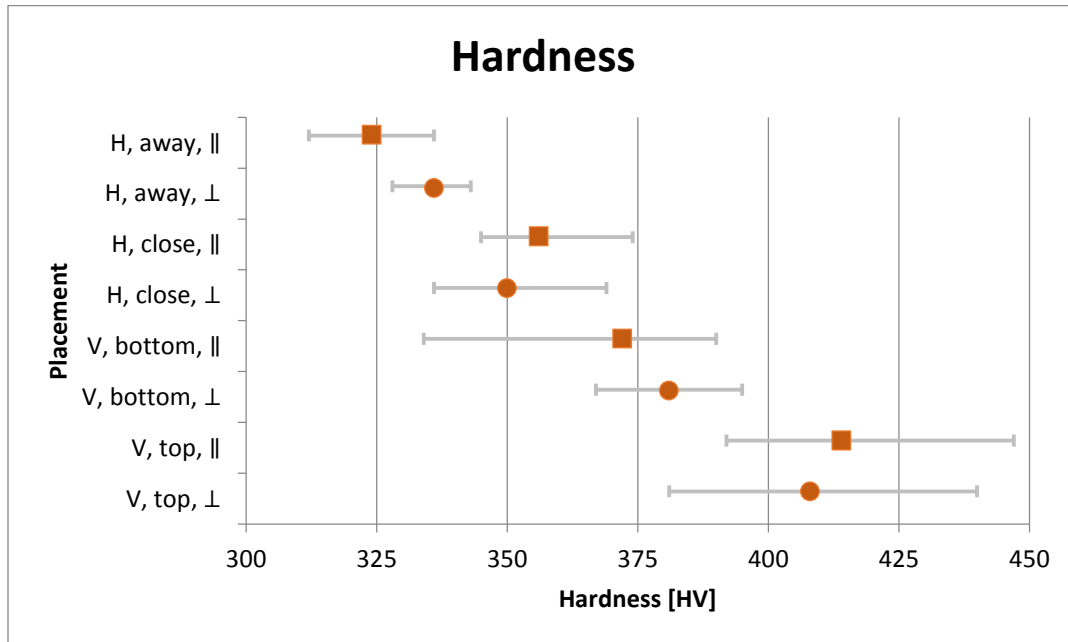


Figure 4.16. Average Hardness value with the variation width marked with a gray line

Some extremes differed significantly from all other measurements. An exclusion of the highest and lowest value of each position results in Figure 4.17 where the variation is significantly reduced for some positions.

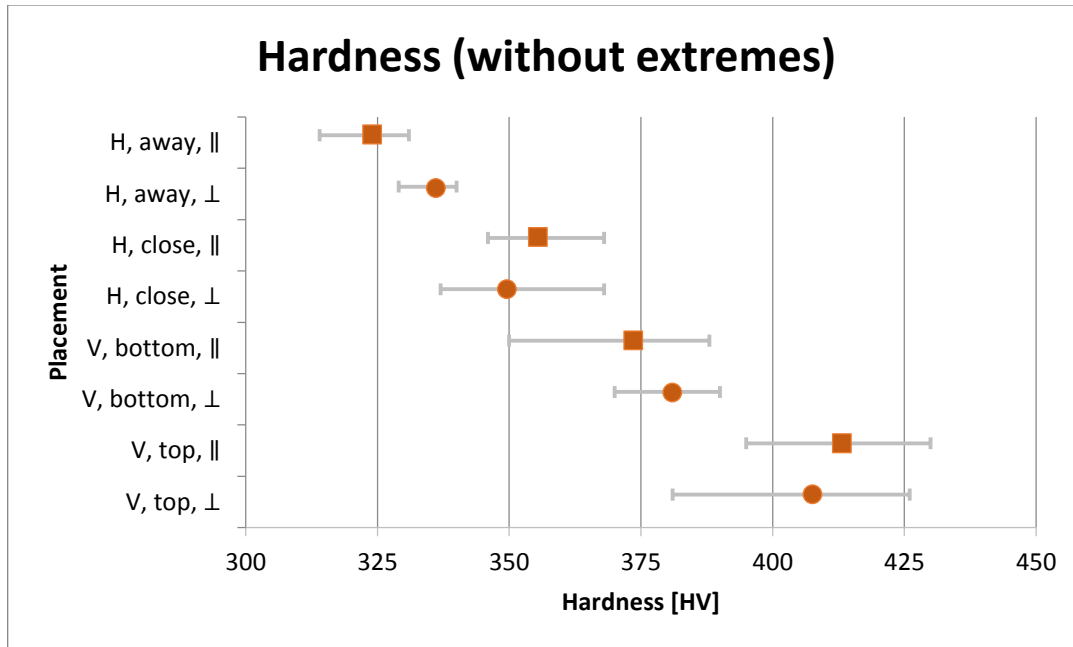


Figure 4.17. Hardness results where lowest and highest result in each position are removed

4.3 Tensile testing

The results from the tensile testing performed at room temperature and at an elevated temperature are presented separately. A summary of all tensile tests in the same stress-strain diagram can be found in Appendix 5

4.3.1 Tensile testing at RT

Table 4.4 presents the results from the tensile testing at RT, the stress-strain curves are found in Figure 4.18. The vertical specimens exhibit a higher yield- and ultimate tensile strength compared to the horizontal specimens but they experience less elongation before failure.

Table 4.4. Results from tensile testing at room temperature

Specimen	$\sigma_{y0,2\%}$ [MPa]	σ_{UT} [MPa]	$\varepsilon @ \sigma_{UT}$ [%]	ε_f [%]
XZ5 (H)	705	1105	24,79	24,94
XZ1 (H)	720	1137	21,26	21,6
XZ6 (H)	643	1019	22,63	22,87
XY1 (V)	1021	1150	10,28	10,46
XY9 (V)	1034	1189	13,1	13,46
XY7 (V)	997	1219	16,6	20,33

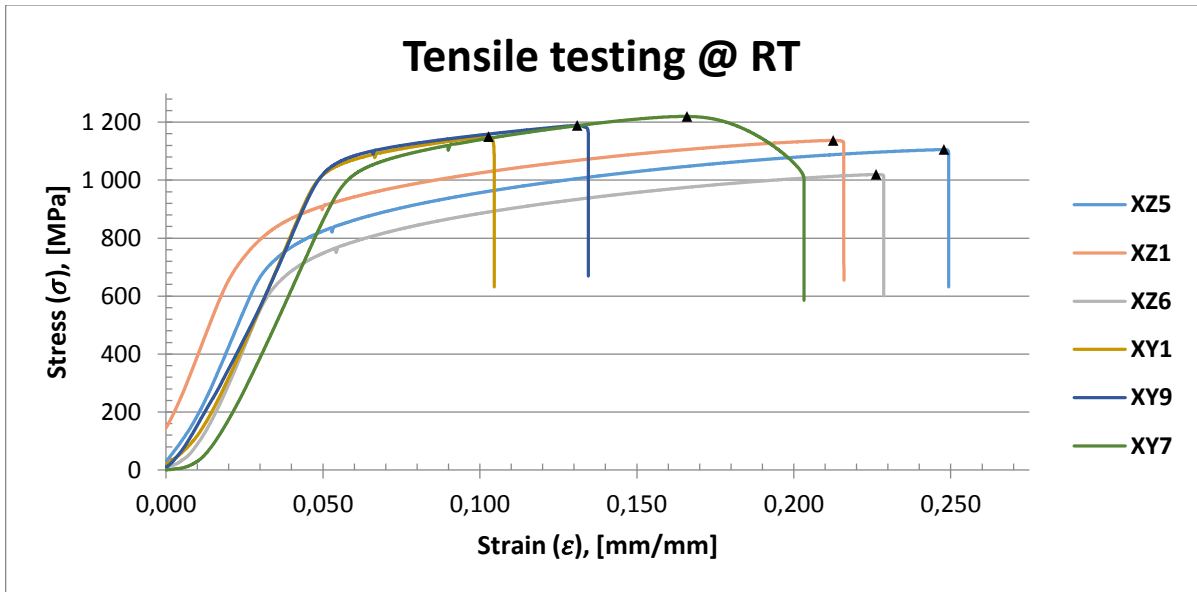


Figure 4.18. Tensile testing at room temperature, stress-strain curve with all six specimens. A clear distinction can be made between the vertical and horizontal built specimens

The vertical and horizontal specimens have been separated in Figure 4.19 and Figure 4.20. The specimens originating from the same BD shows a similar behavior. The difference that stand out the most is the variation in elongation before fracture, especially for the vertical specimens. Another notable thing is that specimen XY7 is the only specimen not fracturing shortly after the ultimate tensile strength is reached but shows a necking before fracture as shown in Figure 4.20.

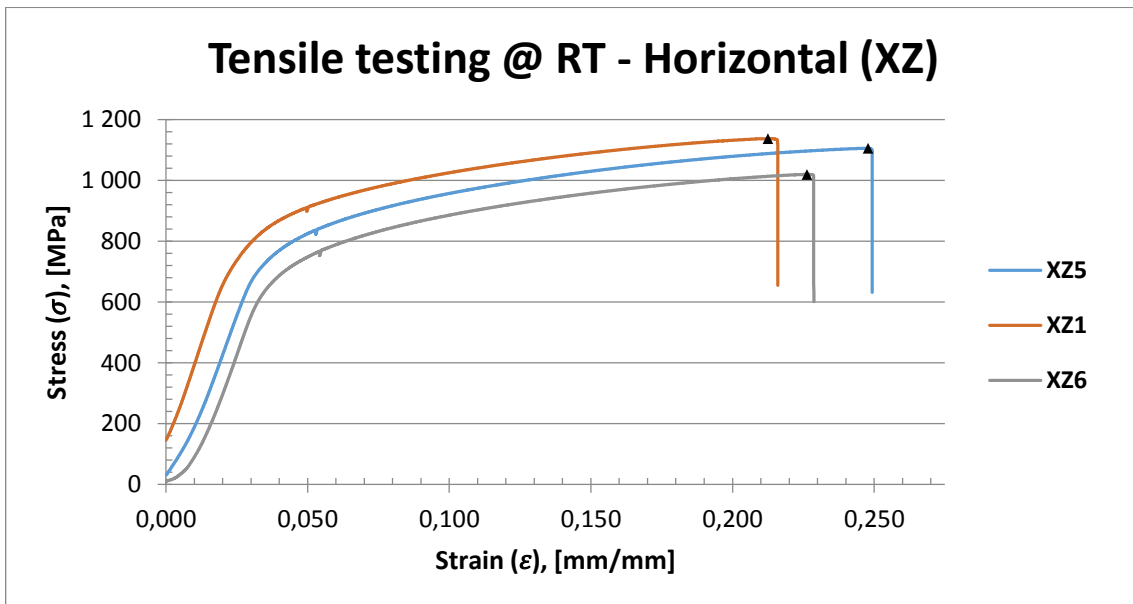


Figure 4.19. Tensile testing at room temperature, stress-strain for the horizontally built specimens. XZ1 and XZ5 have an initial stress due to a negative strain in the beginning of the test

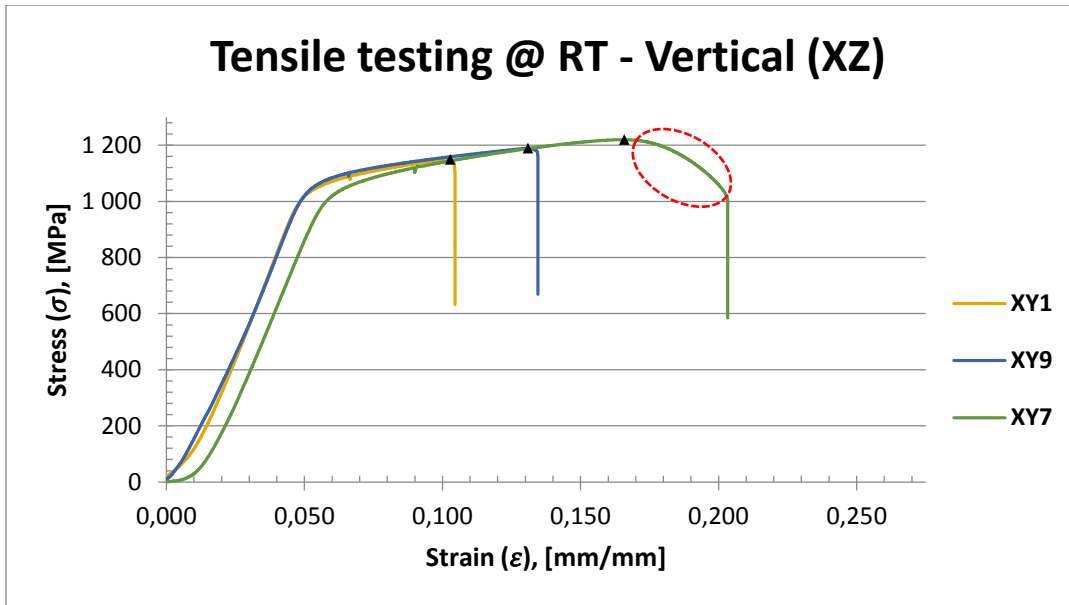


Figure 4.20. Tensile testing at room temperature, stress-strain for the vertically built specimens. All specimens have a similar yield strength and ultimate tensile strength. The biggest variety is the elongation at fracture, which is significantly different between the specimens. The necking of XY7 is marked in the picture

4.3.2 Tensile testing at 650 °C

The results from the tensile testing at 650 °C are presented in Table 4.5 and Figure 4.21. Differences between building directions can clearly be seen. The differences are similar to the testing at RT where a higher ultimate tensile strength is reached in the vertical specimens but with a lower elongation at the σ_{UT} .

Table 4.5. Results from tensile testing at 650 °C

Specimen	$\sigma_{y0,2\%}$ [MPa]	σ_{UT} [MPa]	$\epsilon @ \sigma_{UT}$ [%]	ϵ_f [%]
XZ2 (H)	613	832	11,63	12,70
XZ7 (H)	632	861	11,76	12,61
XZ9 (H)	585	805	10,06	10,78
XY5 (V)	927	972	6,77	10,04
XY6 (V)	897	941	6,68	20,63
XY3 (V)	888	946	6,93	13,09

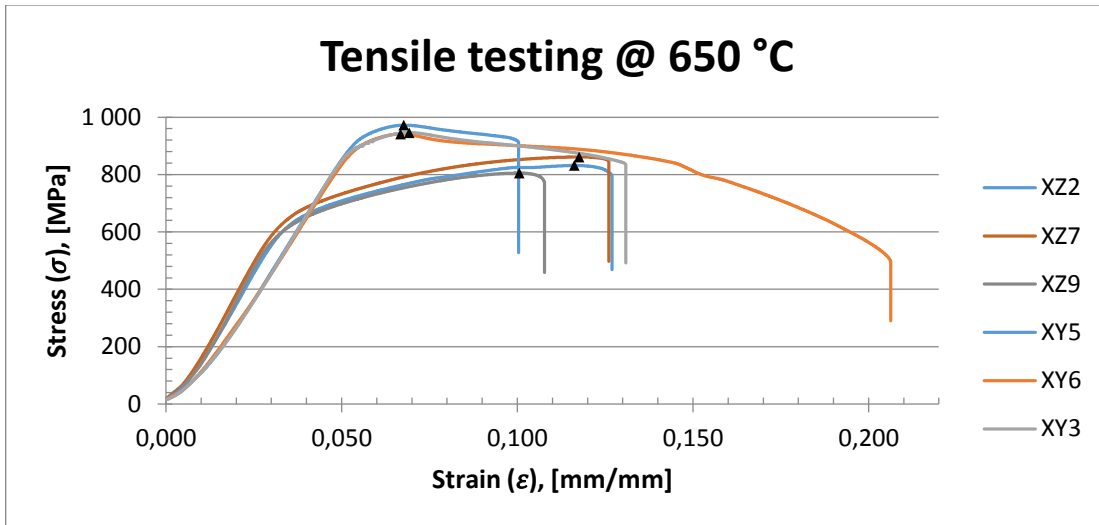


Figure 4.21. Tensile testing at 650 °C, stress-strain curve with all six specimens. A clear distinction can be made between the vertical and horizontal built specimens

The results from the horizontal and vertical specimens are presented separately in Figure 4.22 and Figure 4.23. Noteworthy is the large difference in elongation for the vertical specimens. Specimen XY6 obtained more than twice the elongation than XY5. The horizontal specimens show a more uniform behavior where all have an elongation within two percentage from each other.

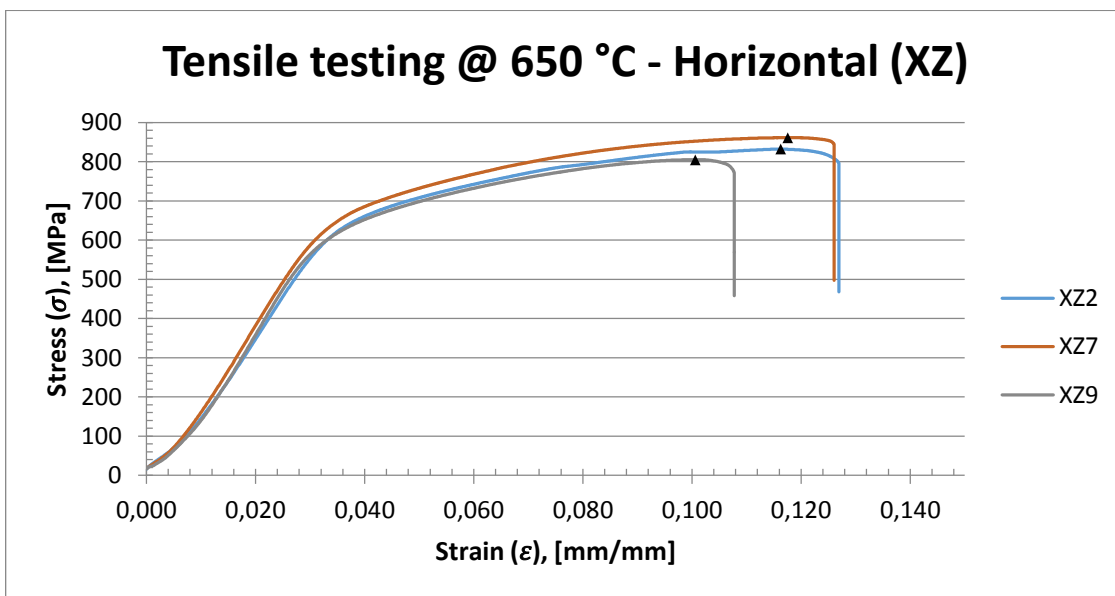


Figure 4.22. Tensile testing at 650 °C, stress-strain for the horizontally built specimens. All specimens exhibit a similar behavior where the biggest difference is the ϵ_f

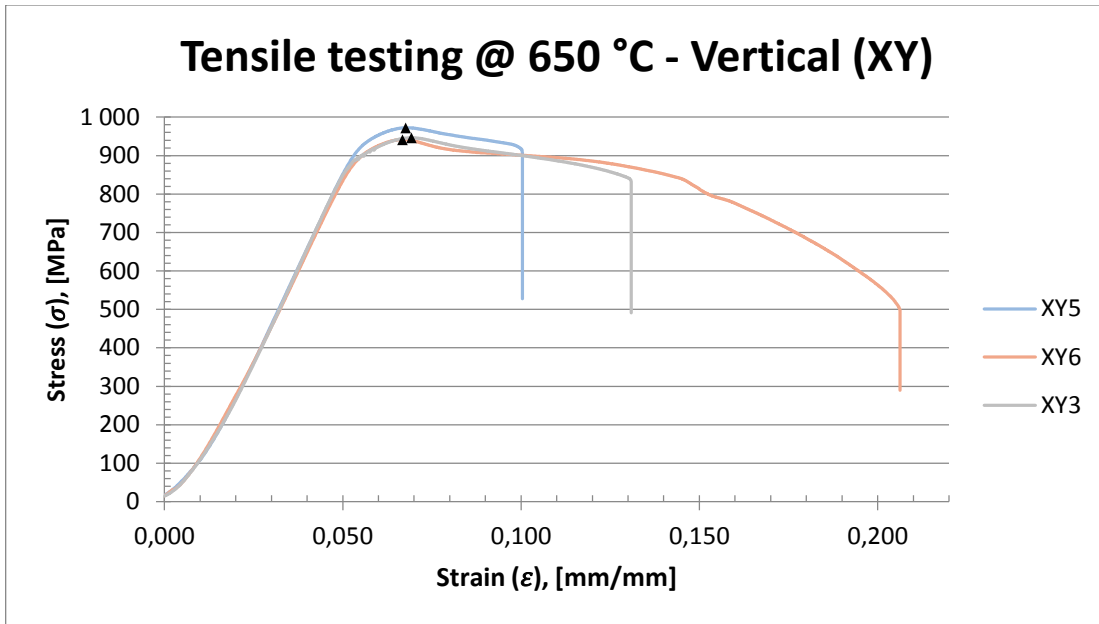


Figure 4.23. Tensile testing at 650 °C, stress-strain for the vertically built specimens. All specimens exhibit a similar strength; both yield strength and ultimate tensile strength. After the ultimate tensile strength is reached the behavior of the samples differ significantly

5 Discussion

5.1 Microstructure

In this chapter, the results of the microstructure examination are discussed.

5.1.1 Grains

The elongation of the grains along the BD shown in Figure 4.1 was expected and mentioned in 2.1.1.2. There are a number of studies exploring different ways of manipulating the microstructure; for example using the scan strategy ^{[19][48]} or the direction of solidification ^[49]. According to Körner et al. ^[50], a smaller line offset might result in more equiaxed grains. A line offset of 150 μm was used to get elongated grains and a line offset of 37,5 μm for equiaxed grains. Another way to affect the grains is the direction of solidification and how the hatch melt is rotated between the layers, where bigger changes in the direction of the hatch melt promotes shorter grains. In the build for this project a line offset of 125 μm was used, which is in the upper range of the offset evaluated by Körner et al ^[50]. The rotation of the hatch melt was set to 180°, which means that the solidification direction only varies in two ways. According to Körner et al. such a setup is likely to result in elongated grains.

When the grain size was studied, it could be established that all studied parts from the bottom of the build (H_{away} , H_{close} and V_{bottom}) exhibit similar structure. This is true both in the average size and in the scatter, according to Table 4.1. The homogeneity at the bottom of the build does not seem to be affected by the BD of the rods. The big difference during the build of the horizontal and vertical rods are the surface area of each layer. The horizontal rods have a larger surface in the BD and more material per layer is therefore added, but it also emits more heat through radiation. V_{bottom} has a smaller area built per layer, but should be affected by heat for a longer time as new heat is added to the rod along the build-process. The horizontal rod is isolated by many layers of sintered powder. However, this does not seem to have an effect on the grains of the material.

The grain structure in V_{top} differs significantly from the rest of the parts with both an almost twice as big average size and a large variation in each specimen. Even the parts of V_{top} with finer grains, like the one shown in Figure 4.2b, are in the larger range compared to the other three sample positions. The areas of V_{top} with larger grains consist of more hard-to define grains, which is shown in Figure 4.2a. These areas with large grains are found in about one third of the pictures taken and no patterns of distribution or placement have been found.

5.1.2 Phases and precipitates

The precipitates in Figure 4.3 and Figure 4.4 were determined to be Nb-rich with the help of EDS and are most likely δ -phase. This is supported by Strößner et al. ^[51] and Unocic et al. ^[52] whom have found δ -phase of similar appearance in AM manufactured IN-718 in their respective studies. Two types of δ -phase were found in this study; grain boundary δ is clearly visible in Figure 4.4b, where larger precipitates oriented in the same direction follows the grain boundary. The other kind of δ -phase is smaller and have precipitated in the matrix of the material and seems to have certain preferred orientations. No γ' or γ'' is visible in the specimens. This is due to a low resolution compared to the size that these phases precipitates in. γ'' usually form precipitates around 60 nm in superalloys according to Donachie ^[6]. This have been confirmed to apply for EBM manufactured IN-718 by Sames et al. ^[12] where an average size of γ' precipitates was found to be 60 nm and two types of γ'' precipitates were 65 nm respectively 35 nm.

The amount of δ -phase in the different parts of the build differed, where Figure 4.5 and Figure 4.6 show the difference in the grain boundaries of the horizontal rods. V_{bottom} have a close resemblance to H_{close} both in number and size of the δ . V_{top} only have little δ -phase in the grain boundaries. The explanation to this is likely temperature variations in the build chamber during the build. The solvus temperature for δ is around 1010 °C and according to Dehmas et al. ^[53] a direct precipitation of δ from the supersaturated matrix can occur around 960 °C. γ' and γ'' precipitates at lower temperatures according to a TTT-diagram for IN-718 ^[54].

One difficulty in knowing the build temperature in EBM is that there are no temperature sensors in the chamber during the build. The build temperature is regulated by an automatic function adding heat to keep the temperature the same. This approximates the heat lead out through the bottom of the build and the heat radiating out of the top of the build. The only reliable temperature is measured under the base-plate, which is 1025 °C in the beginning of the build. These uncertainties open for the possibility that the entire chamber does not hold the same temperature throughout the build.

I think two explanations might be possible for the forming of more δ -phase in H_{away} . It might be an uneven cool down process where H_{away} experiences a longer hold time around the temperature that has the best conditions for precipitation of δ . The other theory is that H_{away} is the coolest parts during the build and might be under the solvus limit for δ -phase. This is based on the previously mentioned heat transfer in the build where the vertical rod keeps being warmed up from the building of new layers, while the horizontal rod is isolated in sintered powder. The heat from the build is led down to V_{bottom} through the vertical rods and some heat might reach H_{close} since the distance between them is narrow. This should leave a temperature difference between the two ends of the horizontal rod, which might result in a difference in the growth of δ -phase. It was mentioned in 2.1.1.2 that a small amount of δ -phase helps controlling the grain boundaries, but this does not seem to have made a difference in the grain size of this build. It is most likely too high amount of δ in both V_{bottom} and the horizontal parts to make a difference. As mentioned in the theory, only small amounts of δ helps. Too much leads to a degradation of the material properties, which might be the case in this study.

Dendritic structures were found in V_{top} shown in Figure 4.7 and Figure 4.8, this was not observed in any other parts of the build. No major investigation on the precipitates found in the interdendritic regions were conducted but some EDS-analysis were made of a few of the precipitates. The results from these analyses showed high amounts of Nb in some and high amounts of Ti in others. This might be explained by findings made by Deng et al. ^[55] who found Nb-rich carbides and titanium nitride (TiN) in EBM manufactured IN-718. Chlebus et al. ^[56] presents SEM images of Laves phase found in grain boundaries and in the matrix of the material. This kind of Laves phase is not present in the material of this study. Another place where Laves phase might precipitate was presented by Kirka et al. ^[57] who has found Laves phase in the same kind of interdendritic regions seen at the top of the build of this study. Since a closer examination in the interdendritic regions has not been made, Laves phase in these regions is not ruled out. Kirka et al. ^[18] presents a theory that the Laves phase dissolves in the material. They found that δ -phase had replaced the Laves phase in the bottom of the EBM-build which had been homogenized. This description fits in to the current study which lack dendritic structure other than in the top of the vertical rods. A further investigation of the precipitates in the top of the build should be conducted before this is ruled out.

5.1.3 Porosities

Porosities of a larger nature that clearly show lack of fusion is shown in Figure 4.9 and Figure 4.10. Unmelted powder particles can be seen and an uneven shape of the porosities. This is due to the process parameters and could probably be avoided if the overlap between the hatch and the contour is increased in the build. The contour constitutes only of a small part of the material and the tensile testing specimen made was produced out of the hatch. Therefore, none of the tests on the material have been done out of the contour, but the hatch has been the main focus. This was already in mind when the rods were built and no major job was done to avoid these types of process-induced porosities.

In Figure 4.9 and Figure 4.10, there are also a few porosities shown with arrows likely to be gas porosities derived from the powder. These porosities have been studied by Sames^[58], who states that the gas can reside inside the powder particles and be transferred directly to the manufactured part. The amount of such porosities has not been studied in this investigation and no comparison to other studies has been made. There is a possibility that the reusability of the powder at University West mentioned in 3.1.1 can affect the powder quality used for this study, which might influence the numbers of porosities in the material. That this will affect the number of gas porosities is however unlikely. Because the powder should not be sintered or melted other than in vacuum in the EBM-process and additional gas pores in the powder should therefore not be formed. More likely, the changes in the powder that cannot be removed when filtered and prepared for reuse can be small oxides on the surface of the powder particles, which may arise from the steps between the processes. These could influence the bonding of the powder particles and possibly lead to a lack of fusion between particles. This kind of lack of fusion would be smaller than those seen in Figure 4.9 and Figure 4.10 and has not been detected in the material.

The most common type of porosity encountered in the material was smaller and irregular in shape; these are shown in Figure 4.11 to Figure 4.15. These are pores formed during the solidification of the material, called solidification porosities. Strondl et al.^[5] has described similar porosities and used the expression porosity stemming. According to Figure 4.12b, this might be an accurate description of some of the porosities found in this studies material with a clear extension along the BD. This kind of pores exist in the contour melt as well but the amount and distribution have not been studied. This type of porosities should be able to be removed with HIP since the size is small and they are formed during the build process and therefore contain a vacuum, making them easy to collapse.

Results from the visual examination of amount and distribution of porosities presented in Table 4.2 shows a striking difference between V_{top} and the rest of the parts. The porosities in V_{top} , shown in Figure 4.13 demonstrates a high concentration of pores in a limited area of Mold 8. This behavior was the same for all studied specimens in V_{top} , but none of the others have such high concentrations. The only pattern found on where in the hatch to these concentrations are is that none was found in the interface between the contour and the hatch.

In V_{bottom} , the linear pattern shown in Figure 4.14 was found and it was first assumed to be only in the bottom pieces of the vertical rods. No pattern was found in the horizontal rods, only what looked like fewer porosities distributed randomly over the hatch. After a review in DF, Figure 4.15, the linear pattern could be seen and measured. The distance between the lines in V_{bottom} matches the distance between the lines in H_{close} and H_{away} . They were measured to be on average 200-300 μm apart, therefore around the double line offset of 125 μm . Sames^[58] explains that these are probably in the middle of a scan pass because it is where the

material solidifies last. Sames encountered the clusters of pores and in one sample the porosities was forming lines as in this study. Sames explains this with the automatic turning point function where the electron beam slows down while closing in on the edge. In the samples of that study, those lines only appear at the edge of the hatch, towards the interface of the contour. This means that the porosities only form when the beam is going out of or into the hatch. A difference between the reporting of Sames and this study is the position in the build where the lines appear. In this case, it is in the bottom of the build in all studied pieces and in Sames reporting it is only in one case, and that is in the top of the build.

This explanation does not seem to match this study, mainly because this linear behavior are found along the whole cross sectional area in many places and not limited to the edge of the hatch. It is more likely to depend on the angle on the electron beam. In welding it is common to use a trailing angle, when the beam is directed towards the finished weld or a leading angle, where the angle of the weld is directed from the welded area. In the case of a trailing angle, more heat is added to the material and the penetration is deeper. In the EBM process, the electron beam is scanned over the powder bed with both the electron beam and the built parts fixed. The beam is angled, resulting in a behavior of both a trailing angle and a leading angle occurring closer to the edges of the build. All the specimens used for the microstructural investigation is built close to the edge of the build plate. According to the hatch melt in Figure 3.4, this means every other line is built with a trailing angle and every other with a leading angle. This can have an effect on the heat input and the cooling rate of the material, which in turn can create these lines of porosities. Another possible explanation is the local stresses that arise in the surface of the material can be relaxed with the formation of these porosities, and then be low enough for the next melt-line to create fewer pores.

5.2 Hardness

No significant hardness differences are observed for measurements \parallel and \perp to the BD. In the differences found, no consistency in which was harder of the two are observed. The differences between the \parallel and \perp surfaces were in all cases smaller than the difference between two different positions. This conclusion is supported by a study of Strondl et al. ^[5] who also determined that no difference was found in their study. However, unlike me, they did not see any difference in the build high in their study.

There are big variations between the different positions in this study. The lowest values are in H_{away} , and the highest in V_{top} . The difference between the average values of each position is more than 20 HV, resulting in a total span of 90 HV, which is a significant difference. What was unexpected to was the significant difference between the different parts of the horizontal rod. V_{top} has distinguished itself in most of the results and it is not a surprise that the results could differ from the rest. However, for all horizontal parts, only small differences have been found prior to the measurement of hardness.

A compilation of other studies displays a width between the results, although some are difficult to compare. Table 5.1 shows that the results from this study are the lowest results of the EBM-results but most of them are higher than the results of SLM. In a study about aging of IN-718, the un-aged material has a hardness of 275 HV and a top-aged material 466 HV. There are major differences between different methods, SLM-manufactured parts have fundamentally different thermal history than the parts made in an EBM-process. The most important comparison may be to the ASM 5662 standard and the minimum requirement of 350 HV. Only 3 out of 4 of the positions in this study are above this limit. ASM 5662 is for

material manufactured with conventional methods. No means of parameter optimization focused on hardness has been made in the build for this study.

Table 5.1. Compilation of hardness values for IN-718. *Average values for each position of sample

Production	Notation	Method	Hardness [HV]
EBM, this study	As-built	HV1	324-408*
EBM ^[5]	As-built	HV0.5	500
EBM ^[55]	As-built	HV0.3	427,5
SLM ^[51]	As-built, \perp to BD	HV10	307
	As-built, \parallel to BD	HV10	341
Heat treated bar ^[59]	Unaged	-	275
	Top aged	-	466
AMS 5662 ^[60]	Aerospace material	-	min. 350

The lowest hardness values are found in H_{away} and could most likely be derived from the conduction of heat in the build. As previously discussed, H_{away} have been isolated more from the heat added later in the process compared to the rest of the positions. These differences in temperature and heat conduction have probably had an effect on the precipitation of γ'' , which is the main strengthening phase of IN-718. In terms of amount and distribution of γ'' , it is only possible, as stated before, to make assumptions due to the fact that these phases have not been studied.

However, a reasonable explanation could be that when the proportion of δ -phase is higher in H_{away} , as discussed in 5.1.2, there may be fewer of the key elements left to precipitate γ'' -phase. According to a study by Acharya et al. ^[60], δ is a softer phase than γ'' , which would explain the lowered hardness results. According to the visual studies, only little δ have been found in V_{top} . This could mean that there may be more γ'' and thus explain the higher hardness in these parts.

In Figure 4.17 where the results are presented without extremes, a big difference in $V_{\text{bottom}\parallel}$, $V_{\text{top}\parallel}$ and $V_{\text{top}\perp}$ can be seen. They still have large variations, but describe a more accurate picture of the distribution. In addition to local differences in materials, which hardness measurement is sensitive to, it may also be due to the inhomogeneity of the material. Two of the surfaces with the biggest variation are both in V_{top} which have a inhomogeneous microstructure in all investigations conducted. The major changes in grain sizes and the clusters of porosities could affect the measurements. When grain size is associated with hardness, small grains give a harder material. This is not true for the current study where the hardest part also has the largest grain. The hardness does not seem to derive from the grain structure of the material and could be more dependent on the precipitation of γ'' .

5.3 Tensile testing

As clearly can be seen in Table 4.4, the V specimens have a higher $\sigma_{y0,2\%}$ and σ_{UT} than the H specimens. This is due to the elongated grains in the microstructure making the material stronger in the direction of the grains. This behavior could be compared to isostress/isostrain

analysis of a fiber composite with an anisotropic behavior depending on the loading direction.

The results for the specimens tested in RT shows a $\sigma_{y0,2\%}$ for the V-specimens at around 1000 MPa and around 700 MPa for H. The σ_{UT} is experienced earlier by the V-specimens but the result is quite close between the two. V is higher in all values but the values for both of the directions are around 1100 MPa. A greater ductility is observed in the H-specimens for all tested specimens with a ϵ_f between 20-25 % while the V-specimens fracture between 10-20 %. All of the fractures have been ductile, but only one sample tested in RT (XY7) has shown significant necking.

The H- and V-built specimens are built in the same build to be able to compare the two directions and minimalizing any differences between different builds. Comparisons between other studies can be difficult, mainly because of the large number of build parameters and automatic functions making it difficult to see significant differences between the builds of different studies. With that in mind, a minor comparison has been made, presented in Table 5.2, only including as-built IN-718 manufactured through EBM and a standard. As can be seen, all EBM studies have similar results regarding $\sigma_{y0,2\%}$ and σ_{UT} . The big difference between the studies is the ϵ_f , where a big variation is found between the studies and the behavior is inconsistent. In this study, a higher ϵ_f is reached in H than in V, which is contradicted by two of the other studies. ϵ_f has a wide span with results from 5,5 % up to 40 %. Sames^[58] has noted major fluctuations in the results of ϵ_f and debates the possibility that it depends on the porosities present in the material, the reason is unknown.

Table 5.2. Summary of tensile behavior from studies conducted on as-built IN-718 manufactured from EBM

Study	Orientation	$\sigma_{y0,2\%}$ [MPa]	σ_{UT} [MPa]	ϵ_f [%]
This study	H	689 ± 46	1087 ± 68	23,1 ± 1,8
	V	1017 ± 20	1186 ± 36	14,8 ± 5,6
Deng et al. ^[55]	H	770 ± 10	1002 ± 15	40 ± 4
	V	921 ± 10	1113 ± 5	31 ± 9
Kirka et al. ^[18]	H	894 ± 24	1061 ± 83	11,5 ± 6,9
	V	925 ± 20	1138 ± 24	15,7 ± 4,3
Strondl et al. ^[5]	H	744 ± 44	929 ± 25	5,5
	V	822 ± 25	1060 ± 26	22
AMS 5662 ^[60]	-	-	min. 1275	min. 12

The results from tensile testing at 650 °C shows a consistency in the differences between H and V, it seems like both directions of the material are affected in the same way. The appearance of the curves are similar to those of the RT-testing. $\sigma_{y0,2\%}$ has gone down approximately 100 MPa on the specimen regardless of direction. The ϵ_f in 650 °C is relatively even for the H-specimens where all tested samples have fractured within 2 percentages. The necking is similar to the necking in RT, with a slight increase for the testing at 650 °C. The V-specimens have a large variation regarding the ϵ_f , which as previously mentioned could be due to the porosities in the material. All the V-specimens show a clear necking after the σ_{UT} has been reached.

V_{top} have previously shown an inhomogeneous behavior not only depending on the BD. This leaves the microstructure in the V-specimens in uncertainty since only the end pieces have investigated further and no knowledge of where the transition from the inhomogeneous top to the more homogeneous bottom occurs. Kirka et al. ^[18] shows that heat-treated specimens displays less fluctuations, especially regarding the ϵ_f .

5.4 Source of errors

In this chapter the sources of error which might have influenced this study are discussed.

A build error was made during the build, the starting angle was accidentally turned 90°. This led to long melt lines in the hatch of the horizontal rods, instead of having the shortest possible melt line across the thin section, shown in Figure 5.1. An automatic feature of the machine has corrected the lines to try to get them as short as possible, resulting in an unknown turning between 5-10°. One thing that this entails is a more difficultly controlled shrinkage during the build. This has resulted in that the ends of the horizontal rods have risen during the build of the first layers, as can be seen in Figure 3.5c. Other potential effects of this is not known.

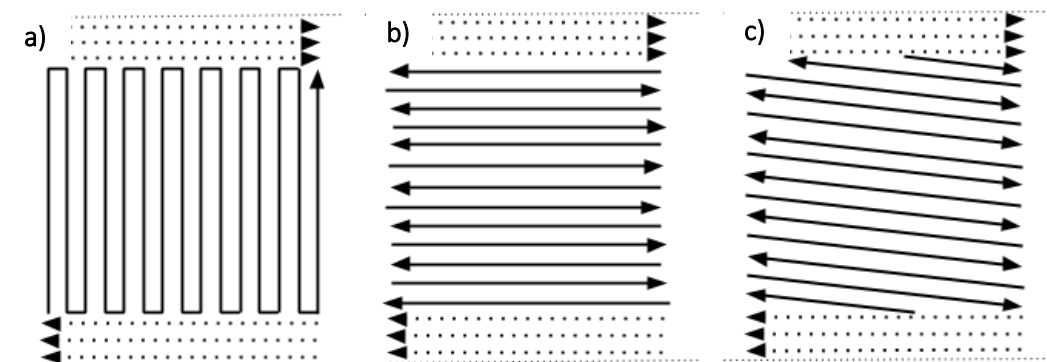


Figure 5.1. Direction of melt lines in horizontal rods. a) as intended. b) as set. c) real case after influence of automatic functions in machine

The build parameters are a source of error. Since this study was carried out on a material built at University West, where EBM is a recent area of research, the build parameters have not been fully optimized. This makes comparisons with other studies about EBM difficult. It is therefore important to keep in mind that the results in this report do not apply to IN-718 overall built with EBM but for IN-718 with these specific building parameters. This, of course, applies to all studies, but the material in this study differs significantly from other more optimized processes, mainly regarding microstructure and number of porosities.

As mentioned earlier, the powder quality could not be ensured because of an ongoing reusability study. As an example, a lower grade of powder could give a reduced flowability, which could in turn affect the number of porosities in the material.

The tensile testing rods used were not of a good quality. The rods had variations in the width over the parallel length of the rods. Some were being slightly cone-shaped that could be seen with the naked eye. There were also problems with the radius of the rods, both between sides of the rod and between different rods. As Figure 3.6 shows, there are also other damages to the rods, many of which are positioned so they should not significantly affect the result.

However, having a non-straight test bar or that the radius of the parallel length differs between rods or different sides of the same rod could have considerable effect on the results.

During tensile testing, no extensometer was used for the samples at elevated temperature. The extensometer normally used was broken. Control measurements of the rods has been carried out retroactively to ensure the results.

When the grain size determination was made, it was in some cases difficult to see the difference between grains and other lines that might occur in the material. It was, in some areas, a difficulty to interpret the grain structure at all. The grain sizes in this study should not be seen as certain, more as a comparison within the specimens and within the build.

5.5 Future research

Here are some examples of possible future studies that would be interesting.

Fractography on the tensile test specimens to further investigate the big variations in ϵ_f . This study could answer the question about the porosities impact on the fracture.

HIP and heat treatment after the build to compare and see which inhomogeneity in the material could be removed. A focus would be on the top part of the rods, which in this study has shown the most inhomogeneity.

A build that continues after the last layer of the vertical rod has been completed. This would leave all the rods in the sintered powder and giving the top pieces the same or similar possibilities of homogenization as the bottom pieces had in this study. This could be a better way to study the anisotropy in the material less dependent on the build-height. This would be an expensive study since the build high is closely related to the cost of the build.

Horizontal specimens build at different build heights. A study if similar differences would be found in horizontal specimens closer to the top as those of the top of the vertical specimens. The radiation of heat would differ and a larger surface is left almost exposed towards the end of the build. This would be interesting mainly because what was most common in this study was a difference due to the height of the build, more than the direction of the build.

Investigations focusing on the scan direction, which investigates the effect of the electron beam angle discussed in 5.1.3. This could answer if measures need to be taken when building parts in the outer edges of the build plate

5.5.1 Future prospects

I think that the future of AM-manufacturing is not going to make all other manufacturing methods obsolete, but serve as a complement to the production systems of the future. This gives an opportunity to use more advanced geometries than is currently possible in components. Complicated 3D-geometries where different parts have different properties without the need to assemble more parts to achieve desired behavior. With a better understanding of the powder recovery, the material waste would be minimized, saving both resources and money.

Another aspect considered promising is to be able to build components with a custom microstructure, where each specific part of a component can have a custom structure to promote a precise need of that part. In the future, a better knowledge of how to utilize the

anisotropy in AM material to meet the needs and, in a complicated geometry, mix anisotropic parts with more isotropic parts in the same component.

5.6 Resource utilization and environmental impact

This chapter tries to highlight some of the aspects regarding resource utilization and the environmental impact of AM-manufacturing.

I experience that the AM methods often are presented as very environmentally friendly, adding materials instead of removing it, like traditional methods. No tool wear during the process is a clear improvement but more material than what is actually built is used in the process. This is often far less than that of traditional methods and powder not used for the build can be reused afterwards. Today the leftover powder are blended with virgin powder. Reusing powder is a separate process that differs between AM-methods. The EBM-method is one of the most time- and energy consuming processes, where used powder is partially sintered and must be separated before sintered and reused. In this area, research is currently being conducted. There are many factors to consider, building atmosphere can affect when some AM methods risk oxidizing the powder and the shape and size of the powder needs to be within the limits for that particular process. A study by Nandwana et al. ^[61] about the EBM-process shows that IN-718 can be reused without much influence of the process. Ti-6Al-4V, one of the most commonly used Ti-alloys, picks up some oxygen but still manages to be reused over a large number of cycles. A large number of cycles is in this study six. However, this is an area that needs to be studied more to find out the effects of recycled powder and each AM-methods limitations in this area. The reusability of the powder is important since this could make a difference between a new production method and an environmentally friendly resource efficient alternative for the future.

One thing worth mentioning is that post processing of components often could be necessary to obtain a serviceable component. In EBM, abrasive blasting must be carried out to remove residual powder, and components must be cut off from support structure and building plate just to have a finished product. Other post-processing is usually conducted as well, in this study for example where circular rods are built and then machined into tensile testing specimens. The surface finish differs between AM-methods and some parts are used without any surface processing. However, to be able to get good fatigue properties, some post processing is needed.

AM provides an opportunity to build more efficient solutions and use complex structures to improve both the production and quality of components. It is important not to forget that AM-manufacturing is a relatively new manufacturing method still undergoing rapid development. Many of today's problems will certainly be solved and developed in the near future. There are great opportunities in the future of AM-methods with many opportunities to improve today's industry, from both a qualitative and an environmental point of view.

6 Conclusions

The anisotropic microstructure found in the material consists of elongated grains in the build direction. This is a typical appearance in the EBM-process derived from the build parameters used in the process. The grain size depends on the build height with larger grains in the top of the build.

Large quantities of δ -phase is found in the material. Dendritic structure exists at the top of the build. Lack of fusion occurs mostly in the interface between the contour and the hatch. Solidification pores are found throughout the material, forming lines in the bottom of the build and clusters in the top.

The hardness of the material is not affected by the direction of the grains but more of the build processes. The temperature of the build seems to differ in the chamber, probably due to the difference in heat conduction through components being built compared to the partially sintered powder. The parts with more δ -phase in the grain boundaries have a lower hardness. The hardest parts are found at the top of the build.

The tensile testing shows that the vertically built specimens have a higher yield-strength and ultimate tensile strength while the horizontally built specimen has a greater ductility. The results regarding the elongation vary a lot without any obvious explanation. The behavior at elevated temperature is lower compared to the room temperature testing but the curves have the same behavior.

The top pieces are consistently different from the others, regarding the microstructure, grain size, porosities and hardness. They also have large variations in the individual specimens, which makes these parts unreliable.

7 References

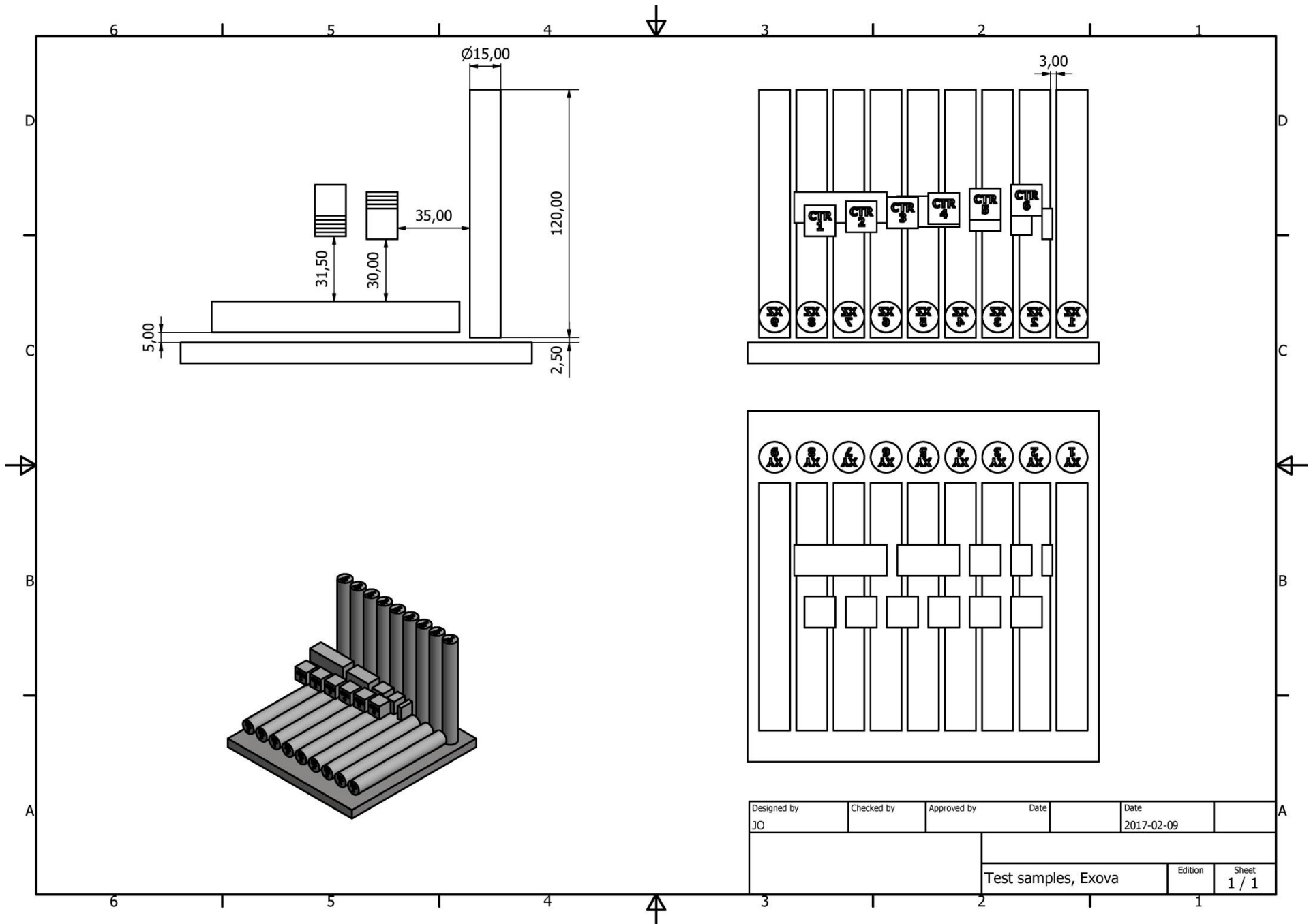
- [1] Exova, "Exova webpage," [Online]. Available: <https://www.exova.com/>. [Accessed 01 February 2017].
- [2] D. Herzog, V. Seyda, E. Wycisk and C. Emmelmann, "Additive manufacturing of metals," *Acta Materialia*, vol. 117, pp. 371-392, 15 September 2016.
- [3] C. Carolin Körner, H. Helmer, A. Bauereiß and F. Singer, "Tailoring the grain structure of IN718 during selective electron beam melting," in *MATEC Web of Conferences*, 2014.
- [4] S. S. Al-Bermani, M. L. Blackmore, W. Zhang and I. Todd, "The Origin of Microstructural Diversity, Texture, and Mechanical Properties in Electron Beam Melted Ti-6Al-4V," *Metallurgical and Materials Transactions*, pp. 3422-3434, August 2010.
- [5] A. Strondl, M. Palm, J. Gnauk and G. Frommeyer, "Microstructure and mechanical properties of nickel based superalloy IN718 produced by rapid prototyping with electron beam melting (EBM)," *Materials Science and Technology*, vol. 27, pp. 876-883, 2013.
- [6] M. Donachie and S. Donachie, *Superalloys: A Technical Guide*, Materials Park, OH: ASM International, 2002.
- [7] L. Murr, E. Martinez, K. Amato, S. Gaytan et al., "Fabrication of Metal and Alloy Components by Additive Manufacturing: Examples of 3D Materials Science," *Journal of Materials Research and Technology*, vol. 1, pp. 42-54, July 2012.
- [8] ASTM International, "Standard Terminology for Additive Manufacturing Technologies," *Designation: F2792 – 12a*, 09 September 2013.
- [9] K. Andrey, L. E. Rännar and M. Bäckström, "Electron Beam Melting: Moving from Macro- to Micro- and Nanoscale," in *Materials Science Forum*, Switzerland: Trans Tech Publications Inc., 2012.
- [10] Arcam AB, "Arcam webpage," [Online]. Available: <http://www.arcam.com/>. [Accessed 18 January 2017].
- [11] Arcam AB, "Arcam Brochure," [Online]. Available: <http://www.arcam.com/wp-content/uploads/justaddbrochure-web.pdf>. [Accessed 18 January 2017].
- [12] W. Sames, K. Unocic, R. Dehoff, T. Lolla et al., "Thermal effects on microstructural heterogeneity of Inconel 718 materials fabricated by electron beam melting," *Journal of Materials Research*, pp. 1920-1930, September 2014.
- [13] W. Yan, W. Ge, J. Smith, S. Lin et al., "Multi-scale modeling of electron beam melting of functionally graded materials," *Acta Materialia*, pp. 403-412, August 2016.
- [14] A. Koptug, L.-E. Rännar, M. Bäckström and Z. Shen, "New Metallurgy of Additive Manufacturing in Metal: Experiences from the Material and Process Development with Electron Beam Melting Technology (EBM)," *Materials Science Forum*, pp. 996-1001, November 2016.
- [15] D. A. DeAntonio, D. Duhl, T. Howson and M. Rothman, "Heat Treating of Superalloys - Cast Superalloy Heat Treatment," *ASM Handbook, ASM International*, vol. 4, pp. 793-814, 1991.
- [16] L. Murr, S. Gaytan, D. Ramirez, E. Martinez et al., "Metal Fabrication by Additive Manufacturing Using Laser and Electron Beam Melting Technologies," *Journal of Materials Science & Technology*, vol. 28, pp. 1-14, January 2012.
- [17] L. Murr, "Metallurgy of additive manufacturing: Examples from electron beam melting," *Additive Manufacturing*, pp. 40-53, January 2015.
- [18] M. Kirka, F. Medina, R. Dehoff and A. Okello, "Mechanical behavior of post-processed Inconel 718 manufactured through the electron beam melting process," *Materials Science and Engineering: A*, vol. 680, pp. 338-346, January 2017.
- [19] E. Cakmaka, M. Kirka, T. Watkins, R. Cooper et al., "Microstructural and micromechanical

- characterization of IN718 theta shaped specimens built with electron beam melting," *Acta Materialia*, pp. 161-175, April 2016.
- [20] S. Kuyucak, "Nickel and Nickel Alloy Castings, Casting," *ASM Handbook, ASM International*, vol. 15, pp. 1119-1127, 2008.
- [21] D. R. Askeland and P. F. Pradeep, *The science and engineering of materials - fifth edition*, Toronto, Canada: Nelson Engineering, 2006.
- [22] D. M. Stefanescu and R. Ruxanda, "Solidification Structures of Titanium Alloys, Metallography and Microstructures," *ASM Handbook, ASM International*, vol. 9, pp. 116-126, 2004.
- [23] H. Helmer, C. Körner and R. Singer, "Additive manufacturing of nickel-based superalloy Inconel 718 by selective electron beam melting: Processing window and microstructure," *Journal of Materials Research*, vol. 29, pp. 1987-1996, September 2014.
- [24] T. Wohlers, T. Caffrey and I. R. Campbell, *Wohlers Report 2016: 3D Printing and Additive Manufacturing State of the Industry : Annual Worldwide Progress Report*, Fort Collins, Colorado: Wohlers Associates, 2016.
- [25] B. J. McTiernan, "Powder Metallurgy Superalloys, Powder Metallurgy," *ASM Handbook, ASM International*, vol. 7, pp. 682-702, 2015.
- [26] R. Reed, *The superalloys : fundamentals and applications*, Cambridge, UK: Cambridge University Press, 2006.
- [27] C. T. Sims and W. C. Hagel, *The Superalloys - Vital High Temperature Gas Turbine Materials for Aerospace and Industrial Power*, New York: Wiley-Interscience, 1972.
- [28] D. Keiser and B. H, "A Review of the Physical Metallurgy of Alloy 718," Aerojet Nuclear Company, Idaho, 1976.
- [29] INSG, International Nickel Study group, "Nickel-Based Super Alloys, INSG Insight – No. 20," April 2013. [Online]. Available: http://www.insg.org/%5Cdocs%5CINSG_Insight_20_Nickel_Alloys_2013.pdf. [Accessed 25 January 2017].
- [30] H. J. Wagner and A. M. Hall, "Physical Metallurgy Of Alloy 718," Defence Metals Information Center, DMIC report 217, Columbus, OH, 1965.
- [31] R. E. Schafrik, D. D. Ward and J. R. Groh, "Application of Alloy 718 in GE Aircraft Engines: Past, Present and Next Five Years," GE Aircraft Engines, Materials and Process Engineering Department, Cincinnati, Ohio, 2001.
- [32] Michlin Metals inc., "Inconel 718," [Online]. Available: <http://www.michlinmetals.com/metal/inconel-718/>. [Accessed 25 January 2017].
- [33] ESPI Metals, "Inconel 718 Composition," [Online]. Available: <http://www.espimetal.com/index.php/technical-data/92-Inconel%20718%20Composition>. [Accessed 25 January 2017].
- [34] ASM Aerospace Specification Metals Inc., "Special Metals INCONEL® Alloy 718," [Online]. Available: <http://asm.matweb.com/search/SpecificMaterial.asp?bassnum=NINC34>. [Accessed 25 January 2017].
- [35] Special Metals Corporation, "INCONEL alloy 718," Special Metals Corporation, Tech. Rep. SMC-045, 2007.
- [36] H. K. Bhadeshia, "Nickel Based Superalloys," Department of Materials Science & Metallurgy, University of Cambridge, 2003. [Online]. Available: <http://www.msm.cam.ac.uk/phase-trans/2003/Superalloys/superalloys.html>. [Accessed 25 January 2017].
- [37] M. C. Chaturvedi and Y. Han, "Strengthening mechanisms in Inconel 718 superalloy," *Metal Science*, vol. 17, pp. 145-149, 1983.
- [38] M. Dehmas, J. Lacaze, A. Niang and B. Viguier, "TEM Study of High-Temperature Precipitation of Delta Phase in Inconel 718 Alloy," *Advances in Materials Science and Engineering, Hindawi*

- Publishing Corporation*, vol. 2011, 2011.
- [39] Y. Desvallées, M. Bouzidi, F. Bois and N. Beaudé, "Delta Phase in Inconel 718: Mechanical Properties and Forging Process Requirements," SNECMA, Materials and Processes Department, BP 81 - 91003, Evry, France, 1994.
- [40] D. G. Brandon and W. D. Kaplan, *Microstructural characterization of materials*, Chichester, England: John Wiley, 2008.
- [41] S. Hogmark, S. Jacobson and Å. Kassman Rudolph, *Svepelektronmikroskopi - I teori and praktik*, 13th edition: Uppsala universitet, 2014.
- [42] K. D. Vernon-Parry, "Scanning electron microscopy: an introduction," *III-Vs Review*, vol. 13, pp. 40-44, 2000.
- [43] Nationalencyklopedin, "Mohs' hårdhetsskala," NE Nationalencyklopedin AB, [Online]. Available: <http://www.ne.se/uppslagsverk/encyklopedi/lång/mohs-hårdhetsskala>. [Accessed 13 February 2017].
- [44] BSI, British Standards, "EN ISO 6507-1:2005 - Metallic materials —Vickers hardness test," Standards Policy and Strategy Committee, 2005.
- [45] R. W. Hertzberg, R. P. Vinci and H. J. L. Deformation and Fracture Mechanics of Engineering Materials, Hoboken, NJ: John Wiley & Sons, Inc, 2012.
- [46] P. K. Neghlani, (*University West*), *Personal communication*, 22 march 2017.
- [47] Struers, "Method number 1429 - Super Alloys, Ni - based (Susp. P/Lub.)," [Online]. Available: [https://e-shop.struers.com/SE/EN/methods/Non-Ferrous_Metals/Nickel_and_Ni_Alloys/Super_Alloys_Ni_-_based_\(Susp_PLub\)\(1429\).aspx](https://e-shop.struers.com/SE/EN/methods/Non-Ferrous_Metals/Nickel_and_Ni_Alloys/Super_Alloys_Ni_-_based_(Susp_PLub)(1429).aspx). [Accessed 14 February 2017].
- [48] R. Dehoff, M. Kirka, F. List et al., "Crystallographic texture engineering through novel melt strategies via electron beam melting: Inconel 718," *Materials Science and Technology*, vol. 31, nr 8: Additive manufacturing, pp. 939-944, 2015.
- [49] H. Helmer, A. Bauereiß, R. Singer and C. Körner, "Grain structure evolution in Inconel 718 during selective electron beam melting," *Materials Science & Engineering A*, vol. 668, pp. 180-187, 2016.
- [50] C. Körner, H. Helmer, A. Bauereiß and R. Singer, "Tailoring the grain structure of IN718 during selective electron beam melting," in *Eurosuperalloys 2014 – 2nd European Symposium on Superalloys and their Applications*, 2014.
- [51] J. Strößner, M. Terock and U. Glatzel, "Mechanical and Microstructural Investigation of Nickel-Based Superalloy IN718 Manufactured by Selective Laser Melting (SLM)," *Advanced Engineering Materials*, vol. 17, nr 8, pp. 1099-1105, 2015.
- [52] K. Unocic, L. Kolbus, R. Dehoff, S. Dryepondt et al., "High-Temperature Performance of UNS N07718 Processed by Additive Manufacturing," in *Corrosion 2014*, San Antonio, TX, USA, 2014.
- [53] M. Dehmas, J. Lacaze, A. Niang and B. Viguier, "TEM Study of High-Temperature Precipitation of Delta Phase in Inconel 718 Alloy," *Advances in Materials Science and Engineering*, vol. 2011, 2011.
- [54] A. Oradei-Basile and J. Radavich, "A Current T-T-T Diagram for Wrought Alloy 718," *Superalloys 718, 625 and Various Derivatives - The Minerals, Metals & Materials Society*, West Lafayette, IN, 1991.
- [55] D. Deng, J. Moverare, R. Peng and H. Söderberg, "Microstructure and anisotropic mechanical properties of EBM manufactured Inconel 718 and effects of post heat treatments," *Materials Science and Engineering A*, vol. 693, pp. 151-163, 2017.
- [56] E. Chlebus, K. Gruber, B. Kuźnicka, J. Kurzac and T. Kurzynowski, "Effect of heat treatment on the microstructure and mechanical properties of Inconel 718 processed by selective laser melting," *Materials Science & Engineering A*, vol. 639, pp. 647-655, 2015.

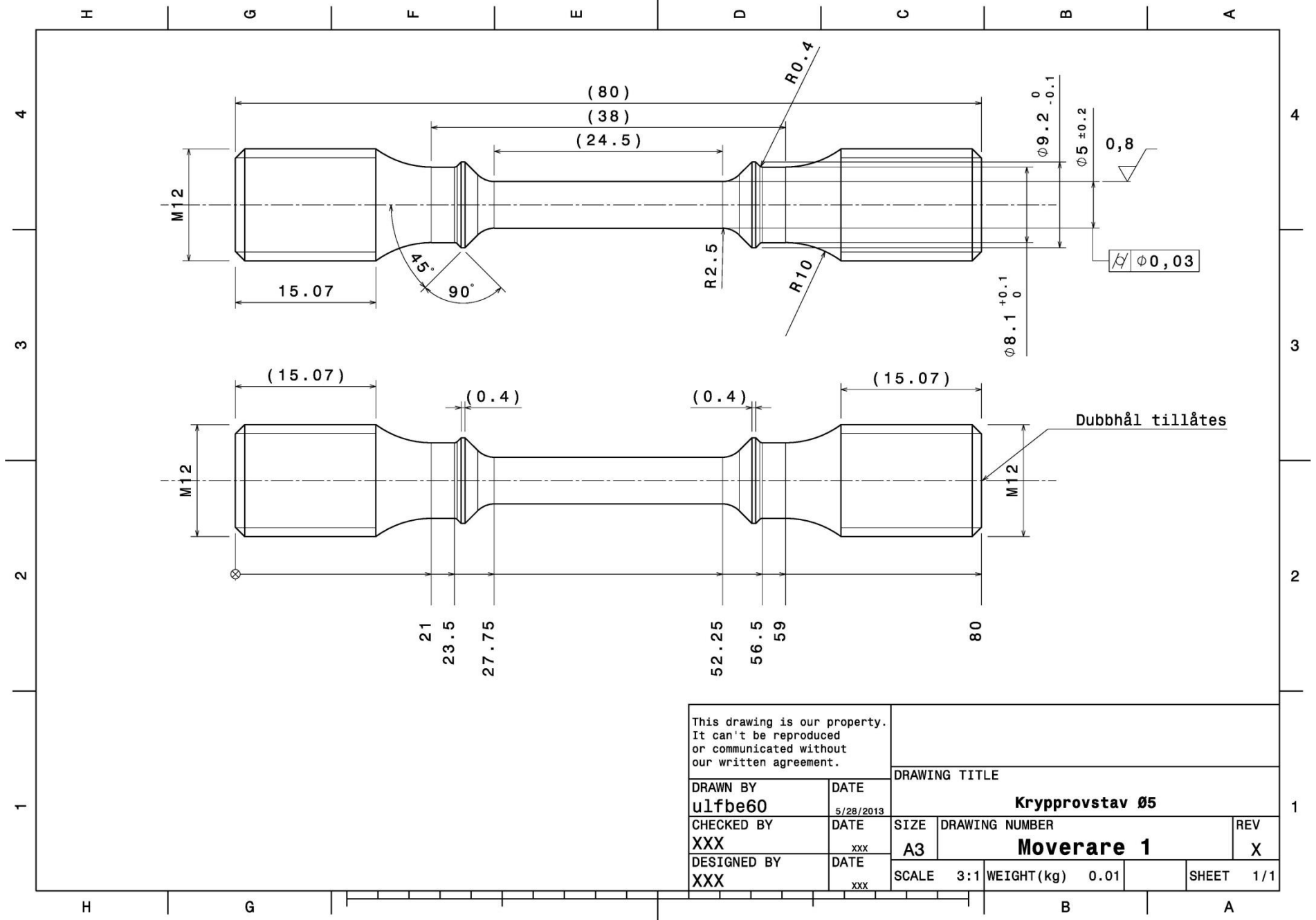
- [57] M. Kirka, K. Unocic, N. Raghavan and F. Medina, "Microstructure Development in Electron Beam-Melted Inconel 718 and Associated Tensile Properties," *JOM - The Journal of The Minerals, Metals & Materials Society*, vol. 68, nr 3, pp. 1012-1020, 2016.
- [58] W. Sames, Additive Manufacturing Of Inconel 718 Using Electron Beam Melting: Processing, Post-Processing, & Mechanical Properties, Texas A&M University, 2015.
- [59] C. Slama, C. Sevant and G. Cizeron, "Aging of the Inconel 718 alloy between 500 and 750 –C," *Journal of Materials Research*, vol. 12, nr 9, pp. 2298-2316, 1997.
- [60] SAE Technical Standards Board, "Aerospace Material Specification - AMS 5662," SAE Technical Standards Board, Warrendale, PA, 2016.
- [61] V. Acharya and D. M. G. Basa, "Microstructural Characterization Of Intermetallic Precipitates In Inconel 718 Alloy By DC Electrical Resistivity Measurements," in *14th Asia-Pacific Conference on Nondestructive testing*, Mumbai, India, 2014.
- [62] P. Nandwana, W. Peter, R. Dehoff et al., "Recyclability Study on Inconel 718 and Ti-6Al-4V Powders for Use in Electron Beam Melting," *Metallurgical & Materials Transactions. Part B*, vol. 47, nr 1, pp. 754-762, 2015.
- [63] ASTM International, "Standard Test Method for Microindentation Hardness of Materials - ASTM E384-16," ASTM International, West Conshohocken, PA, 2016.

Appendix 1 – Drawing of EBM Build (University West)



Designed by JO	Checked by	Approved by	Date	Date 2017-02-09	
			Test samples, Exova		
			Edition	Sheet 1 / 1	

Appendix 2 – Drawing of test specimen for tensile testing (Linköping University)



This drawing is our property. It can't be reproduced or communicated without our written agreement.		DRAWING TITLE		
DRAWN BY	DATE	Krypprovstav 05		
u1fbc60	5/28/2013	SIZE	DRAWING NUMBER	REV
CHECKED BY	DATE	A3	Moverare 1	X
XXX	xxx	SCALE	3:1	WEIGHT (kg) 0.01
DESIGNED BY	DATE			SHEET 1/1
XXX	xxx			

Appendix 3 – Grain size evaluation, results

Table showing the results from the grain size evaluation. All measurements are the average value from the individual pictures in μm

Mold №	H, close			H, away			V, bottom			V, top		
	1	3	5	2	4	6	7	9	11	8	10	12
Picture												
1	34,3	37,5	29,3	32,4	35,3	31,6	37,5	31,6	35,3	200,0	54,5	92,3
2	32,4	37,5	25,0	29,3	41,4	37,5	36,4	34,3	28,6	109,1	120,0	80,0
3	29,3	31,6	33,3	35,3	37,5	31,6	42,9	40,0	35,3	70,6	120,0	66,7
4	29,3	33,3	34,3	30,0	36,4	31,6	35,3	41,4	35,3	52,2	133,3	300,0
5	27,3	30,0	37,5	30,0	35,3	34,3	37,5	40,0	38,7	44,4	48,0	100,0
6	30,8	33,3	38,7	30,8	34,3	41,4	38,7	27,9	34,3	26,7	44,4	50,0
7	31,6	30,8	35,3	36,4	32,4	46,2	29,3	26,7	30,8	41,4	85,7	75,0
8	30,0	31,6	34,3	30,0	40,0	27,3	36,4	31,6	36,4	171,4	171,4	92,3
9	32,4	33,3	41,4	31,6	36,4	37,5	36,4	35,3	38,7	60,0	133,3	54,5
10	31,6	33,3	30,0	37,5	32,4	37,5	41,4	41,4	40,0	41,4	60,0	42,9

Appendix 4 – Hardness testing, results

Table showing hardness testing results

H, close			H, away			V, bottom			V, top		
Mold №	Hardness [HV]		Mold №	Hardness [HV]		Mold №	Hardness [HV]		Mold №	Hardness [HV]	
	∥	⊥		∥	⊥		∥	⊥		∥	⊥
1	357	347	2	336	334	7	380	374	8	407	407
1	362	336	2	330	328	7	379	379	8	420	400
1	359	368	2	323	336	7	350	370	8	411	440
1	359	348	2	325	335	7	366	387	8	410	424
1	355	352	2	319	337	7	374	367	8	430	426
3	364	337	4	315	335	9	388	386	10	404	400
3	374	369	4	331	343	9	334	385	10	428	420
3	348	344	4	328	340	9	377	384	10	413	404
3	350	347	4	326	338	9	382	395	10	429	381
3	368	351	4	329	329	9	390	390	10	447	381
5	346	347	6	326	340	11	377	371	12	392	390
5	365	362	6	312	329	11	371	382	12	400	420
5	345	337	6	314	337	11	369	30056*	12	395	424
5	348	359	6	318	334	11	373	384	12	419	397
5	346	351	6	330	340	11	365	384	12	412	405

* Caused by an error in the machine and is excluded in all results.

Appendix 5 – Tensile testing results, complete

